POLITECNICO DI TORINO

Master's Degree Thesis in Biomedical Engineering

Department of Mechanical and Aerospace Engineering

Characterization of Single Extracellular Vesicles by Atomic-Force Microscopy and Fluorescence Microscopy for Cancer Diagnosis

Supervisor:
Prof. Gianluca Ciardelli

External Supervisor:
Dr. Federico Pevere
Uppsala University, Solid State Electronics
Department of Electrical Engineering

Candidate:
Carolina Paba

Academic year 2019 – 2020

Abstract

Characterization of Single Extracellular Vesicles by Atomic-Force Microscopy and Fluorescence Microscopy for Cancer Diagnosis

Small extracellular vesicles (sEVs) of sizes between 30 and 200 nm are released from almost all the cells of the human body in the extracellular space (i.e. outside the cell of origin). By traveling through body fluids (blood, urine, saliva, etc.) these nano-sized vesicles transport biological information between distant cells in the form of lipids, proteins, RNAs and DNAs among others. This novel way of cell-to-cell communication interaction has been discovered to be important in the development of several diseases, such as cancer development and metastasis. Hence, the study of sEVs is crucial for the early non-invasive diagnosis and therapy of different forms of cancer (e.g. lung cancer).

Although they are nano-objects, sEVs feature a high heterogeneity both in size and in their molecular cargo (e.g. they can contain different types of surface proteins as well as different amounts of those). Consequently, studies aiming at the characterisation of sEVs at the single-vesicle level are very interesting since they can shed light on their biological nature and they can eventually drive their application potential.

In this thesis, we present the characterization of sEVs at the single-vesicle level by performing at the same time size-characterization using an atomic-force microscope (AFM) and surface molecular profiling (markers CD63 and CD9) by means of fluorescence microscopy. The results contained in this work relate to sEVs of the human embryonic kidney engineered cell line (HEK293) but could be applied in the future to clinical samples as well. By correlating the size and molecular profile measurements of single sEVs, we were able to study their correlation which can be important from the biomedical point-of-view.

Contents

Chapter 1

Introduction

Cell-to-cell communication is one of the principal mechanisms by which multicellular organisms are regulated. The exchange of information between cells, via mechanical and chemical signals, affects their behavior, shape, and molecular content. Moreover, it plays a key role in the activation and modulation of fundamental cellular and biological processes, with both positive and negative implications. Indeed, on the one hand, cell communication can take part in tissue regeneration, immune response activation, and blood coagulation. On the other hand, it could also be responsible for tumor development and the exchange of pathogenic agents. Either way, cellular communication allows a vast amount of processes that are crucial for survival [4].

Cell-to-cell communication can be accomplished by either direct cell-cell interaction or by the secretion and transport of soluble molecules, such as growth factors, proteins, and cytokines. Importantly, most cell types release membrane-derived vesicles in the biological environment, which can interact with the neighboring cells and travel towards distant cells for the transmission of biological information [47].

In this regard, over the past two decades a particular type of membrane-derived vesicles, known as extracellular vesicles (EVs), have been investigated [52]. These vesicles have attracted much interest because of their high concentration in body fluids that allow them to travel around the body, acting as an important vehicle of biological information. In addition, they are characterized by high heterogeneous molecular cargo (DNA, lipids, cancer biomarkers), which reflects the status of the parental cell and consequently gives information about the biological environmental conditions [47].

Several bulk methods for the quantification and characterization of these vesicles have been adopted in the attempt to understand their role in the biological process, as well as their diagnostic and therapeutic potential. However, no approaches have succeeded at quantifying and characterizing their wide range of properties at the single-particle level [46]. This is mainly because of their small size at the nano-scale, which requires to perform high-resolution measurements and to combine complementary approaches.

Against this backdrop, this thesis aims at overcoming the major detection limits that affect the techniques that are most prevalent in the field of molecular profiling and size characterization. For these purposes two investigation methods have been adopted, the fluorescence microscopy and the atomic force microscopy. The former is an optical method that uses fluorescence to generate an image of the investigated substances, which cannot be seen by conventional microscopy. In our case, it was used to realize the molecular profiling of fluorescent-labeled proteins expressed by

the vesicles [8]. The latter is an imaging technique used to characterize samples at the nanoscale, for example in terms of size and morphology [41]. In our case, it was used to achieve the size characterization of the vesicles.

Specifically, we took the following steps. Firstly, we tried to estimate the expression level of two tetraspanin proteins, CD9 and CD63, which are considered to be important tumor biomarkers of the EVs. Secondly, we explored the possibility to discern between one single EV and a cluster of multiple small EVs. Thirdly, we tried to investigate whether vesicles' size is a determining factor for their activity in the biological processes, such as the tumor progression, by combining the molecular profile with the size of the single vesicles. In order to validate our single EVs assay, we used vesicles derived from the engineered cell line HEK293 (human embryonic kidney).

The remainder of this thesis is organized as follows: Chapter 2 reviews the relevant literature; Chapter 3 outlines the main phases of the work, with the sample preparation and materials adopted; Chapter 4 describes the experimental method; Chapter 5 presents the main results; Chapter 6 concludes.

Chapter 2

Overview on Extracellular Vesicles

2.1 Extracellular Vesicles

Extracellular vesicles (EVs), are small vesicles in the range of $30 \div 200\, nm$ in diameter, characterized by a cup-shape and a lipid bilayer membrane. They can be secreted by both eukaryotic and prokaryotic cells in pathological or physiological condition, and released into biological fluids by exocytosis. EVs are nanocarriers of multiple surface molecules and functional proteins, but also nucleotides, such as mRNAs, microRNAs (miRNAs), DNAs. EVs are released in almost all body fluids, e.g., prostate secretion, urine, breast milk, cerebrospinal fluid and in blood and plasma, with a reported density between 1.13 and 1.19 g/ml [47], by a complex mechanism illustrated in *Fig. 2.1* [51] that involves the first formation of early endosomes with its subsequent maturation into late endosomes. After that, the inward budding of the late endosome results in the progressive accumulation of intraluminal vesicles inside the multivesicular body (MVB). Lastly, the MVB can take the exocytic pathway, where it can fuse with the plasma membrane and release its contents into the extracellular space [52].

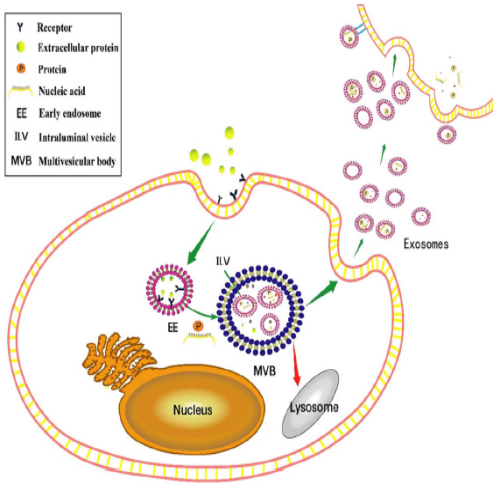

Figure 2.1: Biogenesis and release of EVs: they are formed within the endosomal network and released due to the fusion of the multivesicular body with the plasma membrane [51].

Extracellular vesicles were first discovered in 1967 by electron microscopy measurements. At the beginning, they were identified as merely plasma components released by platelets and designated by Wolf as 'platelet dust' [50]. After one decade was shown that those vesicles were present in the blood as well as in the fetal calf serum and the other body fluids [52]. During the same period was also demonstrated the immunoreactivity of tumor-originated membrane fragments and the presence of multiple proteins involved in intracellular communication. At the end of 90's it was then revealed the mechanism through which they originate [47] and after that, the presence of antigens, RNA and specific surface markers, in the late 2007 [52]. Following all the progress made in the studies of EVs in the last decade, extracellular vesicles are nowadays recognized as potent vehicles of intercellular communication, as mediators of processes such as cell adhesion and immune responses, as nanocarrier from donor to recipient cells, and as important biomarkers in diseases like cancer or neurodegenerative diseases. Due to the high concentration of EVs in biological fluids, liquid biopsy can be performed and this represents a significant advantage for diagnosis and monitoring of those disease like cancer and diseases related to kidney, brain, and cardiovascular system, to whom the traditional biopsy would be very critical and invasive [29]. In the last decade, the number of scientific publications in the field of extracellular vesicles has increased exponentially, as can be seen in *Fig. 2.2* [45], because of their high heterogeneity and membrane composition that can give information about their origin and environmental conditions, but in particular for their important role in the regulation of many physiological functions and cancer metastases and development.

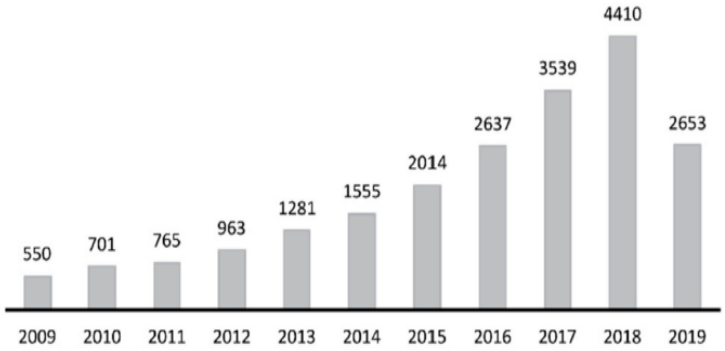

Figure 2.2: Publications trend on Extracellular Vesicles Publications from 2009 to 2019 [26].

Exosomes are nowadays a hot-topic in biomedical science. However, their heterogeneity in size and content, makes it difficult to correctly characterize them and find useful correlations that can lead to a better understanding of their fundamental role in the biological processes. In order to avoid scientific misunderstandings, in the list of minimal information for studies of extracellular vesicles (MISEV) stipulated by the International Society for Extracellular Vesicle (ISEV) in 2014, are summarized the minimum requirements and experimental conditions that must be met to prove the presence of EVs, their activities and the relative effects in the biological environment [45].

2.2 Classification and Properties

Extracellular vesicles classification can be carried out by considering different subgroups: cellular origin, biological function, biogenesis, density, size [4], that all directly depend from the cell type from which they are originated. For these reasons, their classification remains nowadays a bit unclear [47]. *Figure 2.3* illustrates one of the most diffused types of classification, based on the secretion pathway and the size of EVs.

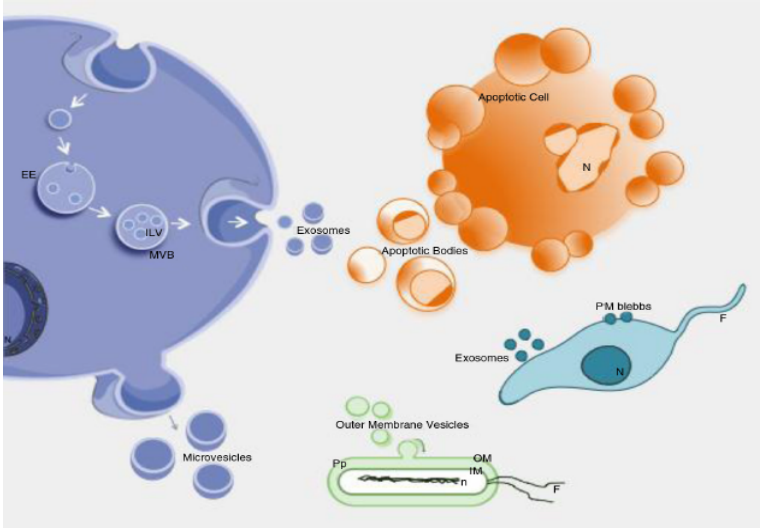

Figure 2.3: Classification of extracellular vesicles [52].

1. Exosomes are identified as cell-derived vesicles, in the range of $30 \div 200\,nm$ with a density around 1.13 and $1.19\,g/ml$, formed by a lipid bilayer that has the origin from the inward budding of the endosomal membrane. Their biogenesis process, illustrated in *Fig. 2.4*, can be divided into four different sequential steps: formation of the early endosome, maturation into the late endosome, inward budding of the late endosome, and the final release of exosomes into the extracellular space [4].

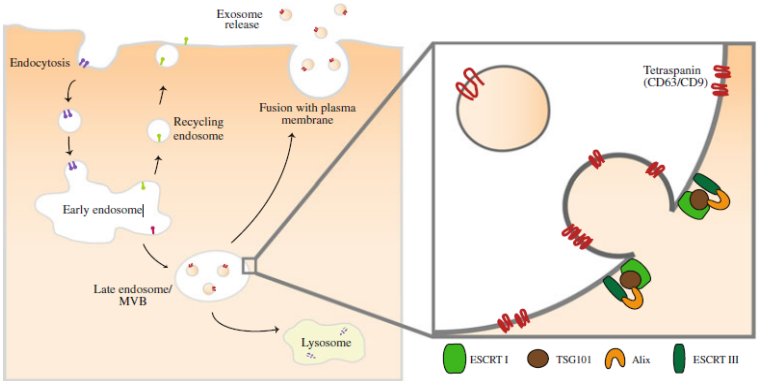

Figure 2.4: Step of vesicles formation and release in the extracellular space [3].

In particular, early endosomes can take two different fates as represented in *Fig. 2.4*. They can either fuse with endocytic vesicles and then undergo a process of recycling and exocytosis, or they can mature into late endosomes. In the second case, it was shown that late endosomes undergo a process of transformation during which small vesicles are inglobated within the lumen of the late endosomes [3] forming the MVB. Once it fuses with the plasma membrane, all the vesicles secreted outside the cell can be classified as exosomes.

2. The term 'microvesicles' identifies a wide group of different types of vesicles, e.g., cellular microparticles, microvesicles, ectosomes, in the range of $100 \div 1000\,nm$, with unknown concentration [47]. As mentioned before, these vesicles are secreted upon direct budding or shedding of the plasma membrane [52], both in normal condition or under a different type of stimuli [29], such as shear forces, hypoxia, changes in Ca level, and mitochondria-dependent stimuli [3]. Furthermore, because of their process of secretion, they are characterized by a high amount of lipid components that are directly derived from the plasma membrane [4].

3. Apoptotic bodies represent the class of vesicles in the range of $50 \div 2\,\mu m$, released during the apoptosis of the cells [3]. Apoptosis is one of the main types of programmed cell death that occurs in multicellular organisms, i.e., autophagy, programmed necrosis, apoptosis. Despite the other mechanisms, apoptosis is a highly regulated and controlled process, fundamental during the organism's life cycle. This mechanism could be divided into distinct steps: condensation of the nuclear chromatin, membrane blebbing, membrane protrusion formation and the final disintegration of the cellular content into distinct membrane-enclosed vesicles identified as apoptotic bodies [6]. The contents of apoptotic bodies, i.e., nuclear fractions, cell organelles, DNA and their development are less explored than the other types of EVs and still not clear ([47], [3])

Table 2.1 summarizes the main classes of vesicles and their characteristics ([47], [53]).

	Exosomes	**Microvesicles**	**Apoptotic vesicles**
Size	$30 \div 200\,nm$	$100\,nm \div 1\,\mu m$	$50\,nm \div 2\,\mu m$
Morphology	Cup-shaped	Cup-shaped	Heterogenous
Density	$1.07 \div 1.18$	Unknown	$1.24 \div 1.28$
Cellular origin	Most cell types	Most cell types	All cell types

Table 2.1: Main characteristics of Exosomes, Microvesicles and Apoptotic bodies.

The focus will now be on the two main and most investigated classes of EVS: exosomes and microvesicles.

As regards exosomes and microvesicles are characterized by similar size, therefore it is not easy to distinguish them unless real-time imaging techniques are used to visualize their biogenesis pathway [45]. If this is not possible, other strategies may be followed. For instance, shape, density, as well as biochemical composition, and cell origin, represent the most adopted criteria to classify the extracellular vesicles ([47],[45]). Both extracellular vesicle types are named based on the cell type of origin. For instance, exosomes secreted by the human prostate gland are called Prostasomes and microvesicles secreted by cancer cells, are named Oncosomes [36].

The main difference between exosomes and microvesicles is the pathway from which they are generated. The first ones come from the endocytic part of the cells and then are secreted outwardly, instead, microvesicles derived directly from the outward budding of the plasma membrane [4]. They also differ in composition because it depends on the pathway by which they are originated. In the case of microvesicles, their composition reflects the ones of the parental cell since they are secreted, as already mentioned, directly from the plasma membrane. In the case of exosomes, their content is transformed, recycled and only a small amount is kept unchanged during all the process of maturation ([47],[4]). It has been shown that both extracellular vesicle types seem to be cup-shaped [47] and they also have in common some contents such as cytoplasmatic and membrane proteins, mRNA and non-coding mRNAs ([36],[3]), but exosomes also contain more complex molecules such as cholesterol, sphingomyelin, and lipid proteins, instead microvesicles contain characteristic platelet receptors glycoprotein exposed in the surface [47]. Moreover, it has been observed that exosomes are characterized by the presence of the class of proteins known as Tetraspanin, e.g. CD9, CD63, CD81, and CD82, where especially the CD9 and CD63 play a key role in the extracellular vesicle formation and tumorigenesis process [4] and they are considered as 'potential biomarkers of exosomes'. Whereas, for the microvesicles, ARF6 and VCAMP3 have been identified as peculiar biomarkers [3]. A summary of the exosome's characteristic molecular cargo is illustrated in *Fig. 2.5*.

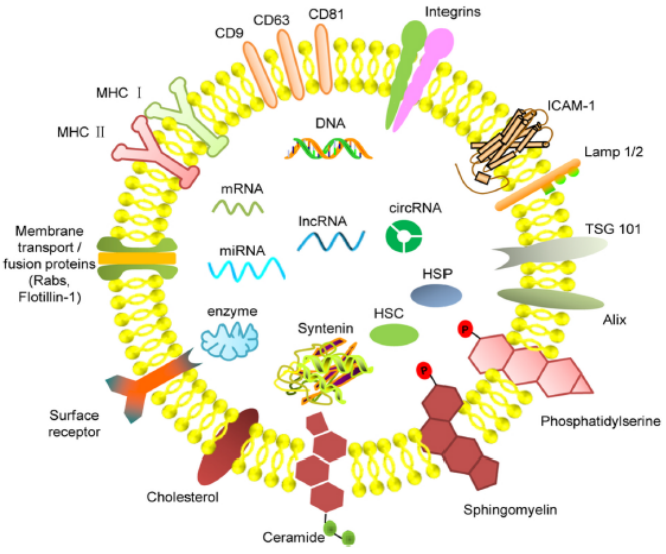

Figure 2.5: Structure and molecular composition of exosomes [24].

Finally, because of the multitude of parameters that must be considered and the incomplete standardization of protocols for the sample preparation and characterization, it is still not possible to classify exactly an EV as microvesicle or exosome, hence a more appropriate nomenclature divides these vesicles into two more general classes: small EVs (sEVs) and microvesicles. From here on, this nomenclature will be adopted.

Focusing now on small EVs potential, it turned out that these vesicles are involved in a large number of different processes, as illustrated in *Fig. 2.6*, such as the intercellular signaling by

modifying the membrane composition of the recipient cells, modulation of inflammatory processes, stimulation tissue regeneration, [47]. sEVs can take part in the transfer of genetic information that can be useful to perform gene therapy [4], and in the maintenance of cellular homeostasis by removing the waste materials and carrying active molecules between cells and tissues [36]. They also exert their potential as nanocarrier of cellular cargo, such as proteins, lipids, and metabolites to the correct final targets [43]. This property makes them suitable for intercellular communication that can have both positive and negative implications. On one side they can be used as innovative delivery systems of drugs or specific molecules to the target tissues and organs [24], but on the other side, it has been shown that they have an active effect on tumor growth progression and metastasis formation [47], by transferring the oncogenic growth factor receptors to the other tumor cells. The tumor expansion is also accentuated by the induction of the angiogenic processes that act as oxygen and nutrients reserve for the tumor cells. The small EVs also take part in the modulation of the immune responses but even in this case, their effect could be either positive or negative. They can, in fact, suppress the immune system or stimulate it in different ways. For example, they can improve the activity of T cells [4], B cells and NK cells [36] which play a key role in the adaptive immune response, or they can moderate the activity and differentiation of monocytes into macrophages or dendritic cells [52]. Macrophages have a pivotal role in the engulfment and digestion of debris, dead cells, and anything that is recognized from the body as an external and dangerous component whereas dendritic cells are considered as messengers of the adaptive and innate immune systems.

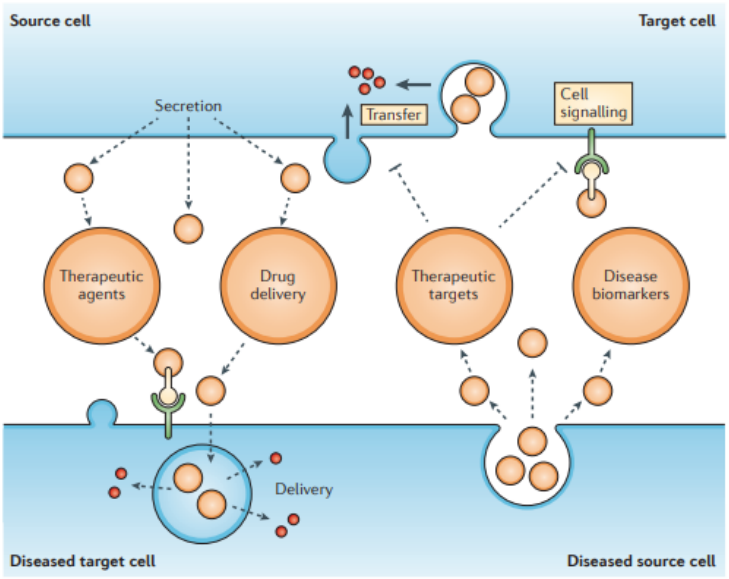

Figure 2.6: Potential of Extracellular Vesicles in biological processes [4].

2.3 Diagnostic and therapeutic potential of EVs

Small extracellular vesicles are considered a promising source of nanovesicles that can be used to perform non-invasive diagnosis and treatment of several diseases such as Alzheimer, Parkinson and Huntington [23]. The intrinsic power as therapeutic agents is related to their bioactive cargo they

contain and transport within the physiological system.

In the last decades, it has been widely observed their excellent potential in tissue regeneration, especially for those vesicles derived from stem cells, with particular attention to the MSCs (mesenchymal stem cells). They are able to moderate and suppress the apoptosis process, are involved in cell proliferation, and take part in the induction of the angiogenic process. Moreover, MSC-derived EVs have a pivotal role in the recruitment and reprogramming of the required cells to perform tissue regeneration. Furthermore, as has been previously described, small EVs take part in the modulation of the immune response and inflammatory process without which tissue/wound regeneration cannot begin. In particular, the inflammatory process must be modulated to avoid the formation of a non-functional tissue that may not integrate into the allogenic environment [49]. One example of small EVs involved in the wound-healing processes are bone marrow MSC-derived exosomes which can stimulate the expression of different growth factors, such as insulin-like growth factor (IGF1), hepatocyte growth factor (HGF) and nerve growth factor (NGF), but are also responsible for increasing the activity of fibroblasts, principal actors together with the inflammation processes, in the tissue regeneration [36].

Another important therapeutic potential of extracellular vesicles concerns the possibility of vesicle-mediated drug delivery against neurological, neuroinflammatory and neurodegenerative diseases [32]. For example, it has been observed their ability to cross the blood-brain barrier (BBB) as they are biocompatible, noninvasive, and they can be both immunologically inert and patient-derived [47]. In particular small EVs have been used for the treatment of neurobiological diseases, as nanocarrier of RNAs species. In order to have a therapeutic effect, RNA must be carried quickly to avoid its degradation in the systemic circulation [36], and it also required non-immunogenic and tissue-specific delivery [47]. Since EVs originate from the major cells of the organism, they are enriched with RNAs species and they can transfer selectively their content to the target cells [49], hence they are considered innovative candidates for drug delivery.

Cell-derived small vesicles are emerging as a new source of clinical biomarkers, that can be used to identify the presence of tumoral cells or to detect the presence of biomarkers expressed in the major diseases since the content of the vesicles reflects the content of their parent cells [35]. For example, exosomes contained in urine or blood of patients with prostate cancer, present the overexpression of prostate-specific antigen; exosome contained in the cerebrospinal fluid of patients with Alzheimer's disease contain phosphorylated Thr181, which is identified as a biomarker of Alzheimer [47]. About this last aspect, it seems that if the EVs contain cytosolic proteins, this could be a signal for the presence of neurodegenerative disease in the patient [36]. Thanks to the high concentration of small EVs in all body fluids, it is possible to extract easily and non-invasively their proteins and biomarker's contents to perform proteomic analysis. Subsequently, is also possible to exploit their ability as nano-carriers to realize patient-based therapies by the modulation of the expression level of the over-expressed proteins [47].

2.4 Main Techniques to study EVs

The main techniques that are currently used to detect sEVs can be divided into three different classes: optical methods, non-optical methods, and digital methods [9]. Because of the high heterogeneity of EVs, usually it is not sufficient to consider only one approach per time, but it is highly recommended to combine multiple characterization methods in order to compare the infor-

mation and results acquired with the different techniques. The parallel use of multiple methods also permits overcoming the limits of resolution and therefore to study the main characteristics of EVs. A shortlist of the main techniques adopted for the characterization of the EVs includes the nanoparticle tracking analysis (NTA) to quantify the number of EVs and their size distribution [9] [19], flow cytometry to measure their physical properties, electron microscopy (EM) to characterize the EVs structure and size, atomic force microscopy (AFM) to characterize the shape [9], the level of adhesion to the substrate and the size as well.

2.4.1 Nanoparticle tracking analysis

The basic mechanism of NTA illustrated in *Fig. 2.7* consists of the detection of the particle's size based on their Brownian motion in a static solution. The particles are under continuous laser beam excitation [12] during which the scattered and fluorescent lights are collected and video-recorded in order to reproduce the individual trajectories of each particle. By the ensemble of trajectories, it is possible to evaluate the size distribution and concentration of the particles [19]. In order to obtain a correct size characterization a long time exposition is required, during which it becomes difficult to maintain constant the temperature and viscosity of the particle's solution [12].

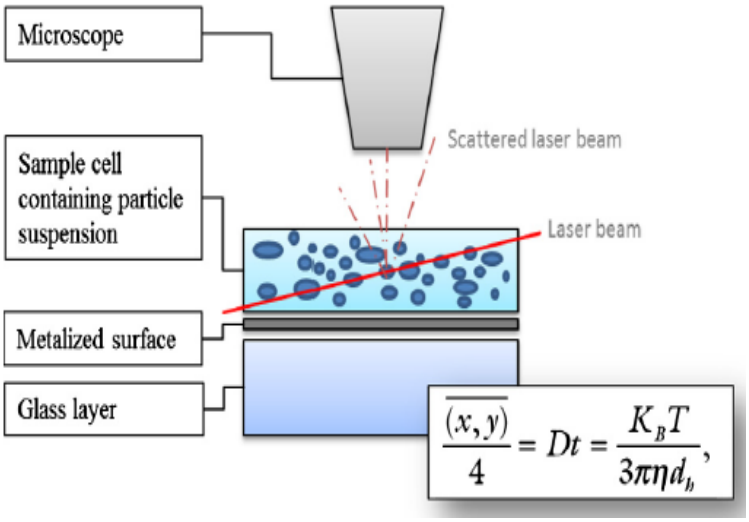

Figure 2.7: Basic principle of detection mechanism of NTA [18].

NTA is one of the most diffused methods for the EVs characterization because [19] it does not require elaborate sample preparation, allows real-time imaging with both unlabelled or labeled particles via photostable probes and can measure particle in the range of $10^7 \div 10^9$ particle/mL suitable for the EVs characterization [9]. As mentioned before, the principle of detection consists on the analysis of the light scattering of the sample, which is related to the properties of the vesicles, e.g. shape and size [19]. Since the scattering light is directly proportional to the sixth power of the diameter, NTA is characterized by high sensitivity for heterogeneous samples. This means that if in the same sample are present vesicles with similar diameters, their scattering signal will be overlapped [9]. For the bigger vesicles the signal it will be amplificated, thereby covering all the signal that would come from the smaller vesicles. Moreover, if the diameter is smaller than

the diffraction limit of the light ($100 \div 500\,nm$), the scattered light will be in the range of the electronic noise, and so the vesicles could not be detectable. To overcome this limit of detection it is possible to support the measurement with non-optical methods. Other possible limits are the intrinsic fluorescence of the background, photobleaching and the labeling of the vesicles. In general, optical methods are characterized by lower resolution compared to non-optical methods. In particular, NTA that it is the most used for size measurements and concentration profiling, it is also the one with the lowest resolution in the size range of exosomes. It is indeed able to detect particle in the range of $30\,nm \div 1\,\mu m$ [9].

2.4.2 Flow cytometry

Flow cytometry (FC) represents one of the typical optical methods utilized for the size characterization of EVs. As for the NTA, flow cytometry can perform the analysis of labeled or unlabeled vesicles but with higher resolution compared to NTA, working in the range of $20\,nm \div 40\,\mu m$, that it is still too large respect to the size of EVs [9]. It has been observed that the most performing flow cytometers can detect particles with a diameter above $200 \div 500\,nm$ [19]. Therefore it is common to observe a shift in the size distribution obtained with optical methods like NTA and FC compared to the results that it is possible to have with non-optical methods that are in general characterized by higher resolution [9].

The basic principle of FC illustrated in *Fig. 2.8* exploits a series of laser excitations paths [19] which focus on the vesicles that are in suspension in a flow chamber. To determine the size of each vesicle, the slope angle of the scattered light is considered. Nevertheless, EVs with a diameter smaller than 500 nm produce scatter light in the range of the electronic noise, therefore as mentioned before, all the vesicles below this value will not be properly solvable [9]. A further limitation

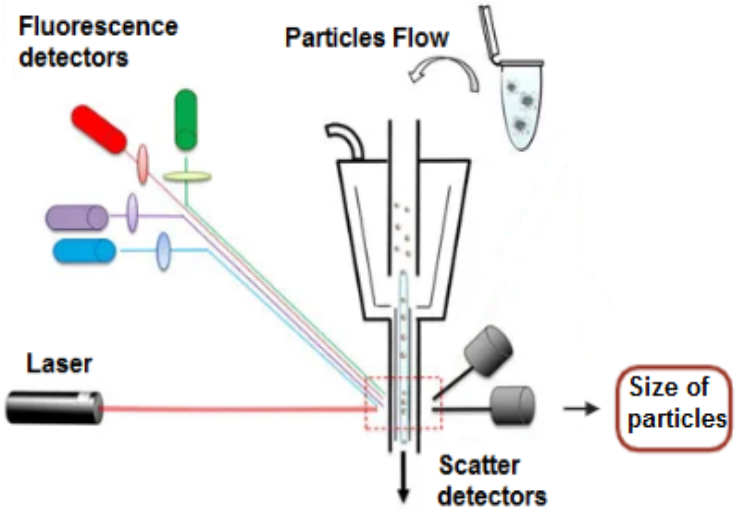

Figure 2.8: Basic principle of detection of flow cytometry [16].

is the concentration of the particles that can be used to detect single EVs, which belong in the following interval $10^7 \div 10^{10}$ particle/mL [9]. For higher concentration it could happen that two

or more small vesicles are simultaneously illuminated resulting as a single bigger spot. This phenomenon, also known as *'swarm effect'* [19] falsifies the real number and the size of vesicles [9]. To overcome this problem is highly recommended to use diluted samples to have a 'linear correlation between the dilution rate and the concentration' [48].

Another commonly used approach could involve the immuno-labeling with fluorescent dyes [48] or the use of magnetic/nonmagnetic beads [9], to carry on biochemical and clinical analysis. It is indeed possible to profile protein and nucleic acids as well as the specific surface markers CD9, CD63, CD81 of EVS [48]. Thanks to its high versatility, flow cytometry remains despite its low resolution, together with the NTA, one of the most popular methods utilized by scientists. Furthermore, custom-built flow cytometers or advance-cytometers with high-sensitivity [9] are often used to minimize the intrinsic artifacts of this technique.

Regarding the progress in this field of research such as the identification of characteristic biomarkers of small vesicles, size characterization, and the related application in the field of diagnostic and biology of EVs, FC could represent a powerful technique, however, it requires customized equipment that increases the costs and reduces the accessibility [19].

2.4.3 Dynamic light scattering

This method is utilized to analyze the size distribution of vesicles in the submicron scale [19]. To obtain this information, the suspension of particles is exited with a coherent and monochromatic laser excitation source [42]. Once the particle meets the laser beam, the light is diffused in all directions and then recorded as a function of time, as shown as in *Fig. 2.9*. The total recording of the scattered light allows discovering the Brownian Motion of the particles. The total recording of the scattered light allows discovering the Brownian Motion of the particles. By processing the signal first with an autocorrelation function and then with a deconvolution function, is possible to determine the size distribution of the hydrodynamic diameter distribution of the particles [13]. In particular, the scattered light changes with the power of 6 of the diameter. However, this information is related to the ensemble of vesicles [19] and does not give any information at the single-particle level.

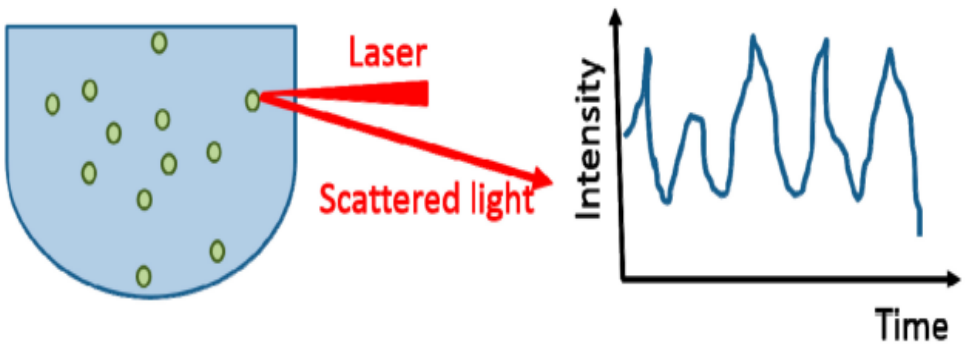

Figure 2.9: Basic principle of Dynamic Light Scattering [42]

Nowadays, the DLS it widely used for the size characterization of the vesicles because it allowed

performing fast measurement with good accuracy, small volumes and without damaging the vesicles, preserving their shape [13]. Nevertheless, it is characterized by a size resolution of $10\,nm \div 6\,\mu m$ and it provides only an average value of the particle's size. Furthermore, the size distribution is strongly altered by the signal coming from larger particles. This masks the scattered light that comes from the smaller particles resulting in an inaccurate characterization [42]. Therefore it can be used only for heterogeneous samples and it is not supposed to be a good approach to analyze extracellular vesicles that are inherently highly heterogeneous.

2.4.4 Fluorescence microscopy

During the past two decades the number of studies based on fluorescence investigation in the field of biology, increase. The most common studies concern the localization and movement of cells and vesicle, genetic and clinical analysis, and DNA sequencing [8]. Thanks to the progress that has been made in EVs investigation and engineering, fluorescence-based techniques are increasingly adopted for extracellular vesicles characterization, with the main purpose of identifying which biomarkers they expressed, and which is the expression level of the surface protein of these vesicles.

One of the reasons why this technique is attracting more attention is that it can allow performing the analysis on the single-particle level uncovering the heterogeneity of results obtainable with the previous approaches. This aspect is important from the scientific point of view since the resolution limits are exceeded, and secondly from the biological point of view because it is not yet clear if there is a direct correlation between the number of proteins expressed on the surface and the size of the vesicles, and if the vesicles which have a higher concentration of proteins are more involved in cellular communication processes or not.

With the optical microscopy-based technique it is possible to detect those EVs larger than the diffraction-limit resolution of the microscope that is $200 \div 300\,nm$, so all the EVs below this range are not detectable and it is not even possible to have any information about their structure. However, it is possible to overcome the limits related to brightfield imaging, performing fluorescence imaging of labeled EVs. For this purpose are available commercial stable fluorophores that can be used to allow the visualization of small EVs [30]. Despite this expedient, it is still not possible to discern between a single bright EV with a diameter smaller than $200\,nm$ and an EV cluster [45], because if several small vesicles are very close or grouped, they will be visible as single fluorescent spot. Moreover, this approach requires the fixation of the sample on a substrate with good optical properties [1], with consequent complication and lengthening of sample preparation [30]. Accordingly to these reasons, this technique is not yet frequently used to perform imaging at the single-particle level but only for the imaging of particle population in suspension. However, despite its limitation, it can provide quantitative images with higher resolution at the single-particle level, compared to the most common methods such as NTA or flow cytometry, with which it is possible to obtain only an underestimation of the EVs counts, size, and the presence of biomarkers in the EV's population [45].

Fluorescence imaging is mostly used to perform real-time imaging of the population of EVs by collecting the signal intensity of the fluorescence coming from the vesicles [8]. It is possible to localize them in the substrate and to quantify the intensity of the signal coming from each vesi-

cle. This information could be afterward correlated to the expression level of a certain surface protein or marker expressed by the vesicles. Moreover, using different excitation sources for different fluorophores, it is possible to characterize for the same sample several markers at the same time, realizing a multiplexed profiling of EVs [19]. At the state of the art are commonly analyzed proteins such as CD81, CD9 or CD63, but also tumor-specific proteins [25]. The final result will be expressed in an arbitrary unit, such as the CCD counts/s, for a specific protein marker in the total EV population, and it will depend on the quality of sample preparation and the acquired image. Therefore, since the final distribution of the acquired signal will depend on all these parameters, it is necessary to collect a large number of data to be able to do a statistical investigation [45].

A widely diffused approach for single EV analysis involves the use of microfluidic systems to carry out multiple targeting of EVs under flow conditions. An example of a typical EV assay (Lee et al., 2018)) utilized for this type of analysis is reported in *Fig. 2.10*. For each imaging cycle, EVs must remain fixed on a substrate, stained with fluorescent antibodies and periodically quenched to perform different fluorochromes [14] coupling for each marker that needs to be analyzed. However, all these steps repeated for a considerable amount of vesicles and markers to detect, require a long acquisition time, that represents the main limitations of this approach. Despite the long exposure time, it has been shown that EVs maintain their structure and the signal quality does not change considerably [25] but also in this case the final results are based on EV population and not on single EV analysis.

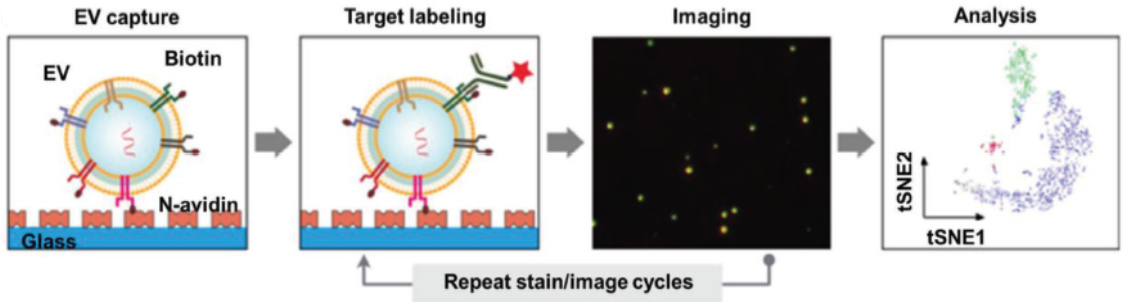

Figure 2.10: Multiplexed Profiling of EVs in a microfluidic system [25].

Some other applications of fluorescence imaging include 'in vivo imaging' that represents the most explored approach to perform high-resolution fluorescence microscopy. It is mainly used to study the biodistribution, uptake, and localization of vesicles in healthy and cancerous organs of the animal body through red/infrared excitation sources that are suitable for the tissues. It can be also used to understand the regenerative potential of EVs released from stem cells such as mesenchymal stem cells, evaluating the difference in the average intensity signal released by treated/untreated organs [17].

2.4.5 Atomic Force microscopy

Atomic force microscopy represents one of the most performing [39] tools to carry out high-resolution measurements of single nanoparticles in the range of $1\,nm$ [19]. The detection principle of this non-optical method is based on the local interaction forces between the cantilever's tip and

the sample [9]. During the scanning of the surface, the attractive or repulsive force is converted into the deflection of the cantilever and recorder by a laser-based detection system. Afterward, this information is converted into an electrical signal to produce the height images of the surface [19].

AFM can be used for biological applications to characterize the structure, composition, biochemical and mechanical properties of biomolecules or cells [40]. Due to the high versatility of this technique, it possible to investigate nanoscale-vesicles in physiological conditions, without the need for coating and specific requirements for the sample. In the case of EVs analysis with AFM, the surface must be chemically modified to obtain the immobilization of the EVs on the surface [31]. The latter must be flat [9], with the roughness under $0.5\,nm$ [31] to clearly discern between the imperfections of the surface and the EVs. In that regard, the typical materials that are used as a substrate for AFM applications are the glass and mica. The latter is used when it is necessary to have a flat background, instead the former is generally selected when good optical properties are required such as for the combined study of AFM imaging and light microscopy.

AFM imaging can be performed both in liquid or in air, depending on the particle's properties. In the case of EVs, it has been shown that the EVs analyzed in air present a characteristic 'cup-shape'. In particular, it seems that they are characterized by a central softer collapsed area respect to the surrounding. The presence of different physical properties between the core and the shell results in different mechanical forces applied by the AFM tip [31]. Whereas in liquid it seems that EVs maintain their spherical shape and their native properties [9]. This can be easily explained considering that the liquid environment could better reflect the physiological environments in which EVs reside.

Another aspect that must be taken into consideration is the strategy of immobilization of EVs on the surface. This could affect the mechanical properties and the size distribution of EVs [47]. At the state of the art, three techniques emerged as the most adopted: deposition on functionalized surface, deposition on antibody-coated surface, deposition on a free surface. It is possible to keep attached the EVs on a free surface only in the case of mica substrate thanks to its residual negative charge which makes possible the electrostatic interaction between the surface and the EVs [41]. In that case, the roughness of the surface does not increase since no other components are added to the surface. However this approach can be used only for charged surface, otherwise, it is necessary to perform further steps to create a residual charge on the surface of materials such as glass (e.g. plasma treatment on glass) [5]. In the case of an antibody-coated surface, there is no limitation in the choice of the substrate, nevertheless, it is more difficult to control the roughness of the surface and the presence of impurities. This approach it is generally adopted when is required a specific binding between the vesicles and the substrate.

The imaging mode is a crucial parameter that must be taken into consideration to have successful single-molecule imaging. Depending on the imaging mode, the forces between the tip and the surface changes. The intermittent contact mode is the most adopted one because it provides high spatio-temporal resolution both in liquid and in air, more accurate force control respect to contact mode and non-contact mode. It is important to optimize the interaction between the tip and the sample to minimize damage and deformation of those soft samples, such as cells and extracellular vesicles [22]. It has been observed that with the increase of the applied force the shape of the vesicle changes. In particular, for forces lower than $1\,nN$, the height measured images show round

vesicles with the diameter in the range of $50 - 70\,nm$. Instead, for higher applied forces above $2\,nN$, the shape is not completely preserved and vesicles appear more flattened with the diameter in the range of $100\,nm$, as shown in *Fig. 2.11* [41]. In addition, with the phase images of vesicles, it has been shown that extracellular vesicles are formed by a central core with higher density and different elastic properties compared the surrounding. This is related to the higher concentration of proteins and mRNA inside the vesicles compared to the surface [41]. However, once the interaction between the tip and the sample ends, the shape is recovered.

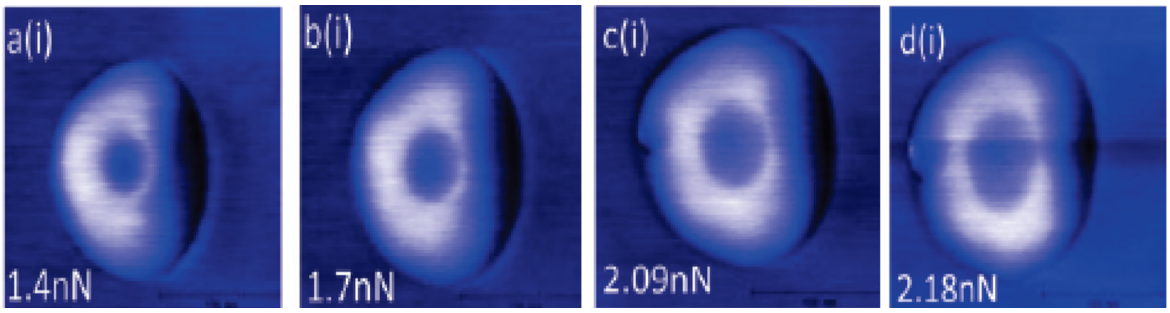

Figure 2.11: AFM-phase image of the mechanical deformation of EVs during the increase of the applied force [41].

With AFM imaging, several tapping mode studies have been conducted on normal and tumor samples in order to highlight their differences. It has been shown that normal and cancer exosomes differ both in size and structure. The first one resides in the range of $40 - 100\,nm$ and presents heterogeneous morphology and density with also intravesicular aggregation. Instead, exosomes from cancer cell line do not have a marked difference in density between the core and the shell, are characterized by a wider distribution of diameter that varies in the range of $20 - 400\,nm$, and their morphology it is not predictable because it can be either irregular or circular as for normal exosomes [40].

Concerning the aforementioned aspects, with the AFM it is possible to perform an articulated analysis of extracellular vesicles at the subnanometer resolution, in terms of morphology, mechanical properties, size, and chemical composition, without irreversibly altering the properties of the sample. Thanks to the high versatility of this technique it is possible to characterize single exosomes all-around, discerning between healthy or cancer cell lines. For these reasons, ISEV always suggests combining high-resolution imaging techniques such as AFM, with the other technique utilized for size and concentration measurements, in order to reduce evaluation errors and the level of uncertainty [19].

The principles of detection of both Fluorescence Microscopy and Atomic Force microscopy will be explained in detail in the *Chapter 4*.

2.5 Goal of the thesis

The purpose of this thesis is to address the resolution limits of detection for vesicles' analysis at the single-particle level. To that end, we will estimate the molecular profiling of surface proteins of

small Evs, through fluorescence microscopy measurement. In particular, the proteins we will devote our attention to are the following: CD63 and CD9, both belonging to the family of tetraspanin membrane proteins. The rationale behind the choice of such proteins is that they are considered important biomarkers of small EVs. Moreover, this thesis will also attempt to characterize vesicles' size in a physiological condition by using atomic force microscopy. Finally, we will combine the two aforementioned imaging techniques, namely, fluorescence microscopy and atomic force microscopy, in order to: first, tackle the difficulty of distinguishing between one single EV and a cluster of multiple small EVs; second, investigate the correlation between vesicles' size and their molecular profile at the single-particle level. Such correlation will be investigated to understand whether vesicles' size is a key determinant of communication between vesicles and of their active role in tumorigenesis processes. The sample that will be used in this thesis is composed of the vesicles derived from the Human Embryonic Kidney 293 (HEK293) cell line.

Chapter 3

Single-EV assay

This chapter reports how is articulated the single-EV assay implemented to realize our single-EVs characterization, with the description of the sample preparation and the main materials adopted to perform the experiments.

The *Figure 3.1* illustrates the general guideline followed during the experiments and it consists in the first EVs capture onto a D263M Schott glass disk (*ibidi gridded glass coverslip*) with a thickness of 170 μm and a diameter of 28 mm, characterized by grids at a repeated distance of 500 μm, in 4 different areas of the disk. It was decided to use this type of substrate due to its quality and small thickness that allow performing super-resolution microscopy measurements, but also for the presence of the grids that were ideal for our single-molecule characterization, since they allow to localize the EVs and to perform their single detection in a defined area, for repeatable measurements. The surface was activated with (3-Aminopropyl)triethoxysilane (APTES) and Glutaraldehyde (GA) that act as a linker between the substrate and the EVs. The immobilization of the EVs was necessary to perform the imaging in a liquid environment and with high resolution. After the EVs capture, it was decided to realize the antibodies labeling only for the multiple protein profiling performed with fluorescence microscopy.

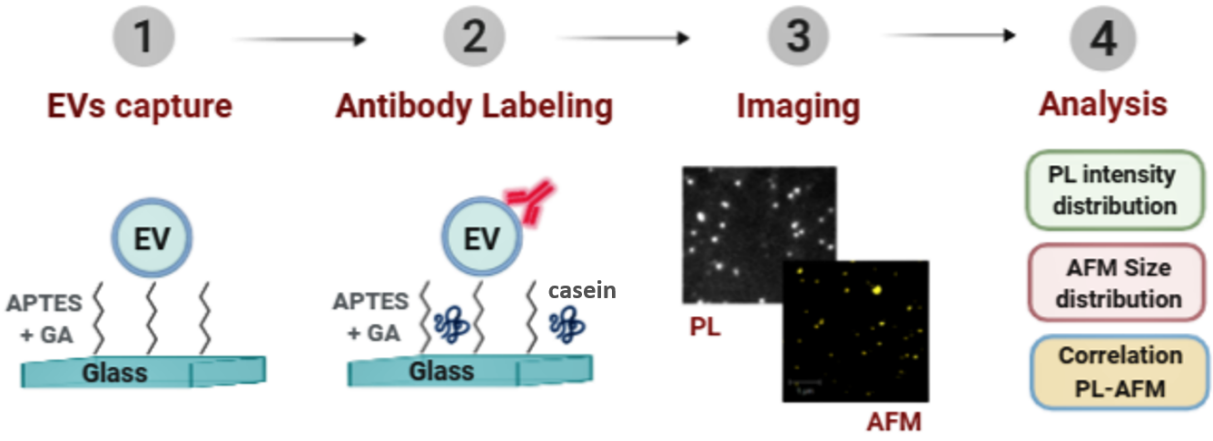

Figure 3.1: Our single-EV assay adopted for single-EV characterization.

After the first part of the sample preparation, two different characterizations have been carried out, one with a photoluminescence setup, for the protein profiling of the vesicles, and one with the AFM for the size characterization. The respective images obtained from these two measurements were then analyzed in terms of photoluminescence (PL) intensity distribution and AFM size distribution. Finally, once the PL and AFM parameters were optimized and the vesicles were well characterized, it was decided to combine the two investigation method to find which correlation exists at the single-particle level, between the expression level of the vesicles and their size.

3.1 Sample Preparation

The sample preparation, illustrated in *Figure 3.2*, includes the first functionalization of the glass substrate, the consequent addition of EVs (provided by the collaborating group led by S. El Andaloussi at Karolinska Instutet (Stockholm)) and, depending on the type of experiment, the blocking of the free binding sites and the final binding of fluorescent antibodies on top of the vesicles.

1. **TL1 cleaning**: This step is used to activate the surface with the exposition of OH groups, and also to remove all the impurities that may be present on the glass surface since any kind of contamination would be visible in both the photoluminescence and AFM images and can determine the increase of the background noise, limiting the observation of single EVs.
   To realize the cleaning, the glass is immersed for $10\,min$ into a TL1 cleaning solution whose temperature is kept at $88°\,C$. The TL1 solution is a mixture of H_2O, H_2O_2, NH_3 respectively in proportion $5:1:1$ in volume. After that, the glass is rinsed first in de-ionized water and then in ethanol, for a few minutes.

2. **Silanization process**: This step consists in the formation of a silan-monolayer on the substrate, with the exposition of NH_2 groups [44]. To carry out the silanization, is prepared a solution of 5% APTES ((3-Aminopropyl) triethoxysilane) in ethanol (EtOH). After 1 minute of hydrolyzation, the glass substrate is kept immersed for 10 minutes in the APTES solution. Thereafter the sample is rinsed first in ethanol and then in de-ionized water, for a few minutes.

3. **Incubation in Glutaraldehyde (GA)**: Glutaraldehyde acts as a linker between the modified glass slide and the vesicles, thanks to the exposure of CHO groups on both sides. One end binds to the NH_2 groups of the surface, whereas the groups on the other side remain free for the following steps.

   The glass slide is dipped for $1\,h$ in $1\%\,GA$ dissolved in $1\times PBS$ (Phosphate-Buffered Saline), followed by rinsing in de-ionized water (DIW) for a few minutes.

4. **EVs binding**: The EVs are first diluted in $1\times PBS$ to reach very low concentrations for single-EV studies. To prevent agglomerations, the sample is vortexed for $20s$ after each dilution step. The dilution rate depends on the initial concentration of the stock and the type of analysis. For combined AFM-fluorescence imaging, it is suggested to use lower concentration compared to the concentration that can be used to perform only fluorescence imaging. The adopted concentration range varies between $10^8 \div 10^9\,particle/mL$. The optimize incubation time for the covalent binding between CHO groups of GA and NH_2 groups of EVs is $1\,h$, at the end of which is recommended to do a good washing with $1\times PBS$.

The next two steps are performed only when it is necessary to obtain the antibody binding. Otherwise, the functionalization process ends with the binding of the EVs, as it is shown in *Fig. 3.2(A)*.

5. **Deactivation of GA**: A solution of tris-ethanolamine (triETHA: $0.1\,M$ tris-buffer and $50\,mM$ ethanolamine, $pH = 9.0$) it is used to deactivate the non-specific binding site of GA that remained free after the incubation step of the exosomes. Without this step, the subsequent binding of the antibodies would be non-specific and would increase the image background. The suggested incubation time is $30\,min$, at the end of which tri-ETHA is rinsed with $1 \times PBS$.

6. **Saturation of residual free binding sites**: In this step, a casein-based blocking solution ($0.05\,w/v\,\%$) is prepared to saturate the residual free binding sites. This step required $1.5\,h$ of incubation to completely minimize the non-specific binding of antibodies. At the end of the incubation, Casein is rinsed a few times with $1 \times PBS$.

7. **Antibodies binding**: Antibodies are diluted in $1 \times PBS$. The dilution rate depends both on the type of antibody and the EV sample that is used. It is recommended to try different concentrations to find the best one for each sample. After $1\,h$ of incubation time, the antibodies are rinsed with $1 \times PBS$.

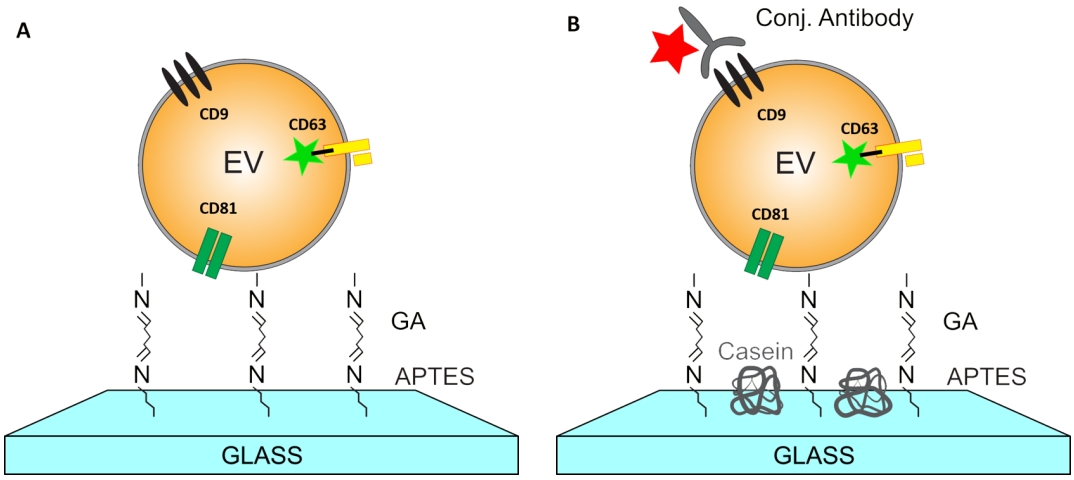

Figure 3.2: a. Functionalistazion done up to step 4; b. Functionalization done with all the 7 steps.

During all the sample preparation is important to keep the sample hydrated, otherwise EVs can detach and the functionalization may not be homogeneous.

A more detailed illustration of the sample preparation process, with the chemical groups involved, is provided in appendix A.

3.2 Materials

- **Substrate and rubber well**: The substrate that we used to perform the experiments was a glass coverslip (previously described in detail) of $28\,mm$ in diameter with Ibidi grids

($50\mu m$ pitch). We decided to use this substrate to be able to do repeatable measurements. Furthermore, with the use of a rubber well (as shown in *Fig. 3.3*) it was possible to perform 4 different measurements, one per well, where two wells were commonly used to analyze two different samples, or to test the same sample with different functionalization procedures, whereas, the two remaining wells were used as control. At the end of the sample preparation, each well was filled with 1×PBS.

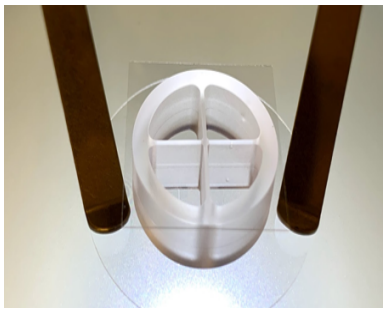

Figure 3.3: Single-EV assay for photoluminescence measurements, formed by a glass coverslip as substrate and a rubber formed by 4 well for multiple analysis in liquid.

- **Sample**: The main sample that was analyzed with uPL and AFM measurements were the EVs derived from the cell line HEK293 (human embryonic kidney cells grown in tissue culture, provided by KI). This cell line, stably expressing CD63 and CD9, was transfected to overexpress the CD63 fused to its C-terminus with the mNeonGreen fluorescent protein (mNeonGFP) [7].

  To perform all the experiments, the initial stock solution of $50\,\mu L$ at $6.6 \cdot 10^{12}\,particles/mL$ was diluted in multiple aliquots of $40\,\mu L$ at $6.6 \cdot 10^{10}\,particles/mL$ and stored in freezer.

Starting from each aliquot, serial solutions were carried out to reach the desired concentration. Each aliquot has been used to perform individual experiments as it was observed that the sample tended to degrade or form agglomerates.

- **Antibodies**: CD9 antibody conjugated with Alexa Fluor 647 (AF647) has been used to do photoluminescence measurements using a red laser with $\lambda = 632\,nm$ at $5\,mW$ as excitation sources. The initial volume was $100\,uL$ with a concentration of $6.67\,uM$ and molecular weight of $150\,kDa$.

- **AFM-tips**: NANOSENSORS qp-BioAC probes designed for imaging in air and liquid of biological samples have been used to perform the AFM measurements. They are made with a quartz-like material and partially coated with a reflective layer of gold. The typical size are: radius around $10 \div 20\,nm$, tip height of $7\mu m$, and thickness of $370 \div 430\,nm$.

Chapter 4

Experimental Method

4.1 Photoluminescence (PL) measurements

Fluorescence microscopy is one of the most advanced investigation methods in the field of in vivo and in vitro studies for the characterization and visualization of biological components [28] such as tissue, cells, proteins, single molecules, and for the study of the typical biological phenomenon in which they are involved. For this purpose, different fluorescent probes, such as fluorophores and fluorescent proteins, but also new methods of target labeling have been investigated and optimized to perform high-resolution imaging without damaging the target biological component [20]. Regarding the single-molecule analysis, one great advantage provided by the fluorescence imaging is that the signal intensity of the fluorescent probe is directly proportional to the concentration of the target molecules, allowing their quantitative characterization. Fluorescent proteins (FPs) represent in that case the widely adopted fluorescent probes for multiple reasons e.g., their high heterogeneity in the light spectrum from the ultraviolet (UV) to the infrared (IR), their versatility in the genetic encoding, good stability in the biological environment, and optimal brightness, that depict them as a powerful fluorescent probe [28]. On the other hand, the new generation of fluorophores, such as Alexa Fluor probes, are characterized by higher quantum yield, high photostability and cover a wide range of the light spectrum, as well as the (FPs) [21]. In our study, as it will be illustrated in the following sections, were adopted two different fluorescent probes, the mNeonGreen and the Alexa Fluor 647, for the multiple profiling of two different proteins, CD63 and CD9 respectively.

4.1.1 Basic principles

Figure 4.1 shows the basic mechanism of fluorescence microscopy. The specimen placed on a stage on top of an inverted microscope is first excited with a light source at a specific band of wavelengths, and the emitted light by the sample is afterword collected. By using a dichroic mirror (DM), the excitation light can be directed towards the sample and then filtered once it comes as scattered light from the sample. In this way, only the excitation light (which retains physical, biological or chemical information) can reach the detectors. More in detail, regarding the excitation light, before reaching the sample, it first passes through a dichromatic beamsplitter placed at $45° C$ respect to its direction that selects and reflects only the light at the desired wavelength. After that, before reaching the collector, only the emitted fluorescent light will be collected by the objective and directed toward the collector, passing through an emission filter and a second mirror placed

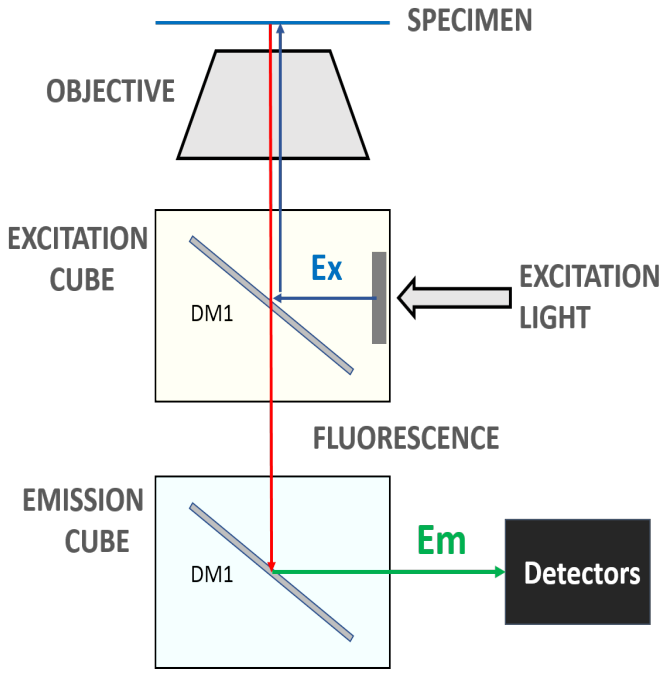

Figure 4.1: Basic scheme of fluorescence microscopy.

at 45° respect to its direction [27]. For these reasons, the selection of the appropriate filter for a successful fluorophore excitation, and the choice of the correct objective for the emitted light collection, represent the basis for good imaging.

For the fluorescent imaging of the biological component of interest, it is necessary to realize the selective labeling of the target with fluorescent probes, such as commercial fluorophores or fluorescent proteins, that can be excited at specific wavelengths and are characterized by high fluorescent quantum yield. This parameter represents the fluorophore's efficiency in converting the excitation light into fluorescence. In particular, the fluorescent emission depends both on the concentration of the fluorophore in the sample, and on its absorption and emission characteristics [27]. For what concerns the fluorescent proteins, two more parameters, such as the pH-sensitivity and the photobleaching rate, must be taken into consideration [28].

In our case, it was decided to use two different fluorescent dye, the Alexa fluorophore 647 (AF647), and a mNeonGreen fluorescent protein (mNeonGFP). AF647 is characterized by a high quantum yield, good signal stability for a wide pH range, and specific targeting for a variety of proteins, antibodies and peptides, with the typical excitation range between $594\,nm$ and $633\,nm$ and the maximum emission at $665\,nm$ [1] that can be image by filtering the signal with a long pass filter. The mNeonGreen protein, derived from a tetrameric fluorescent protein from the Branchiostoma lanceolatum, is one of the brightest and stable protein, characterized by high quantum yield [38], a suited excitation at $506\,nm$ and a maximum fluorescence emission at $517\,nm$ [2] that can be filtered using a standard GFP band-pass or long-pass filter for the imaging of labeled component. It was decided to use the mNeonGreen instead of the GFP since it produces higher signal inten-

sities with a typical brightness 3 times greater than GFP, and it is more stable and less sensitive compared to GFP [28]. It was decided to use these two different fluorescent probes both for their ideal characteristics that allow performing high-quality images and also for their different working excitation/emission wavelength that was an essential condition for the parallel analysis of the two different biomarkers.
Table 4.1 reports the details of the two fluorescent probes adopted for the expression level profiling of the CD63 and CD9 proteins.

	Excitation	**Emission**	**Quantum Yield**	**Lifetime**	**Target protein**
AF647	650 nm	665 nm	0.33	1 ns	CD9
mNeonGreen	506 nm	517 nm	0.8	3.1 ns	CD63

Table 4.1: Technical characteristics of AF647 and mNeonGreen adopted as fluorescent probes for the profiling of the protein CD63 and CD9 ([1], [2]).

Regarding the optical parameters that must be optimized to perform high-resolution quantitative imaging of the fluorescent protein, the excitation power, transmissivity of the optical system, the efficiency of the fluorophore, objective aperture and camera resolution and sensitivity affects the overall sensitivity, resolution and signal-to-noise ratio. In particular, the numerical aperture of the objective determines the resolution and the brightness of the image, by collecting the fluorescence emission of the sample. In order to improve the quality of the image, it is necessary to use the highest numerical aperture which allows both to collect the largest number of photons, but also to resolve the sample at a fixed distance [34].

4.1.2 PL setup

In this section will be illustrated the photoluminescence (PL) setup used to measure the emitted light from the single EVs. With photoluminescence one refrs to the phenomenon of light emission by a sample that is photoexcited with a light source at a certain wavelength and can be divided into two different classes: phosphorescence and fluorescence, depending on the time in which the light is emitted. This phenomenon in our case can be referred to fluorescence, where the light emission stops immediately when the excitation is switched off [33].

The schematic view of the setup used to perform the characterization of the sEVs is shown in *Fig. 4.2*. The core of the system is an inverted microscope connected to a thermo electrically-cooled CCD camera that works at $-100° C$ to minimize the CCD dark counts and can detect single-photon events. For the excitation sources, a blue LED light with $lambda = 455\, nm$ was used. The major advantages of the blu LED are that an LED is not as expensive as a laser, it is quite stable and it allows illumination of a wide area with good temporal power stability. The possibility nowadays to use different LED sources which can be switched in $\sim 100\, \mu s$ allows the simultaneous labeling of many biomolecules. The LED light could reach the sample through the lens of the microscope in bright-field configuration (BF) and once collected by the objective, was always filtered with GFP filter cube composed of an excitation filter (Exc), a dichroic mirror (Di) and an emission filter (Em). The light was then directed toward a CCD camera passing through a second mirror. Finally, the image was acquired by Andor Solis software for image capture and analysis. For the acquisition three different parameters were varied: exposure time that must be

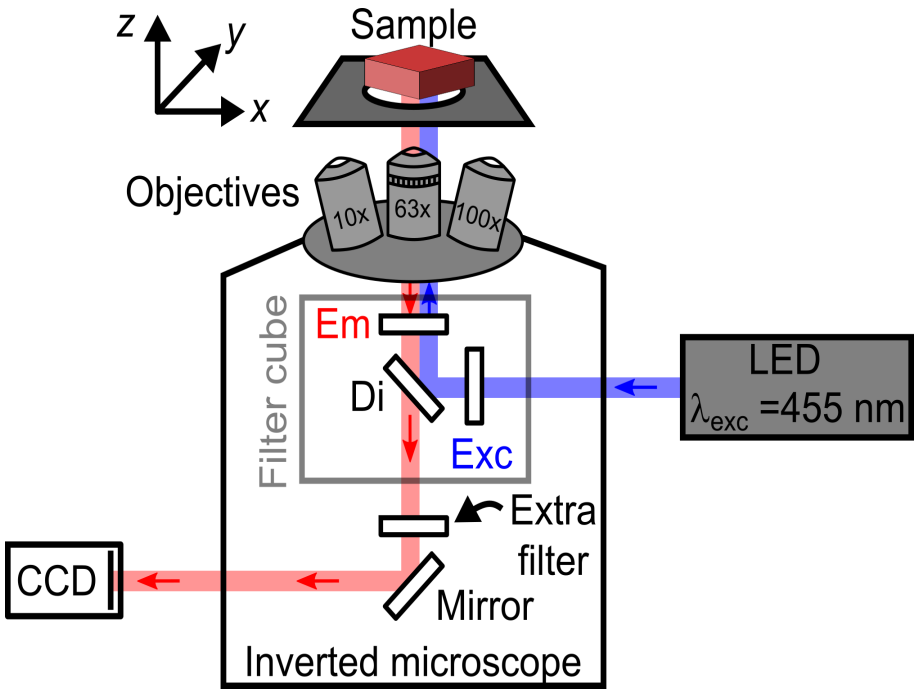

Figure 4.2: Schematic view of the micro-photoluminescence setup used in this work.

selected to do not reach the saturation, the pixel shift and the electron multiplier (EM) gain level which represents the multiplication factors of the signal. The signal coming from the incident photons on the detector, are first converted to electrons and then multiplied by the EMG level. On top of the microscope, three different objective lenses were mounted based on the type of test that had to be done. The lens with 10x magnification (Zeiss,= 0.25 and field-of-view 1.3 mm), and 63x with glass-thickness correction (Zeiss,= 0.75 and field-of-view 200 µm) were used to perform only photoluminescence imaging, instead, the lens 100x oil (Nikon) was used to collect the images for the combined PL-AFM analysis. The main difference between each objective is the numerical aperture which quantifies the amount of light that can be collected and the ability of the objective to resolve fine specimen detail for a fixed object distance that will be shorter with the increasing of the magnification [34]. The resolution of the objectives is important as well since we want to match the diffraction limit, which is the ultimate limit for fluorescence microscopy. Since the numerical aperture (NA) directly depends on the refractive index of the medium between the objective and the specimen, it is possible to obtain higher NA replacing air with immersion oil for example, that has a refractive index of 1.51.

4.1.3 PL Imaging (data acquisition and processing)

The PL measurements were performed on the inverted microscope setup shown in *Figure 4.2*, with a 10x and 63x objective, using Andor Solis software. Regarding the acquisition parameters, an acquisition time of $10\,s$ with $EMG = 20$ and EGFP filter cube selected. Instead, for BF acquisition an EMG of 6 was adopted. Every single imaging cycle consisted in the acquisition of three images: excitation spot, the background/control and finally the images of small EVs.

The image analysis was performed using ImageJ and Matlab. The excitation spot image was first filtered by averaging neighbor pixels to reduce the noise. Such image was then imported in MATLAB where the excitation LED spot was fitted using a 2D Gaussian profile, see Fig. 4.3(a). Unsuccessful fittings were usually overcome by additional filtering of the high-frequency components of the spot image. An image called "Normalization factor", as shown in *Fig. 4.3(b)* is then created from the fitting and allows to correct each PL image from the excitation spot non-uniformity by simple image pixel-by-pixel multiplication. The intensity correction of the PL image was made using a plugin of ImageJ, by multiplying the normalization factor obtained in the previous step with the PL image of the EVs.

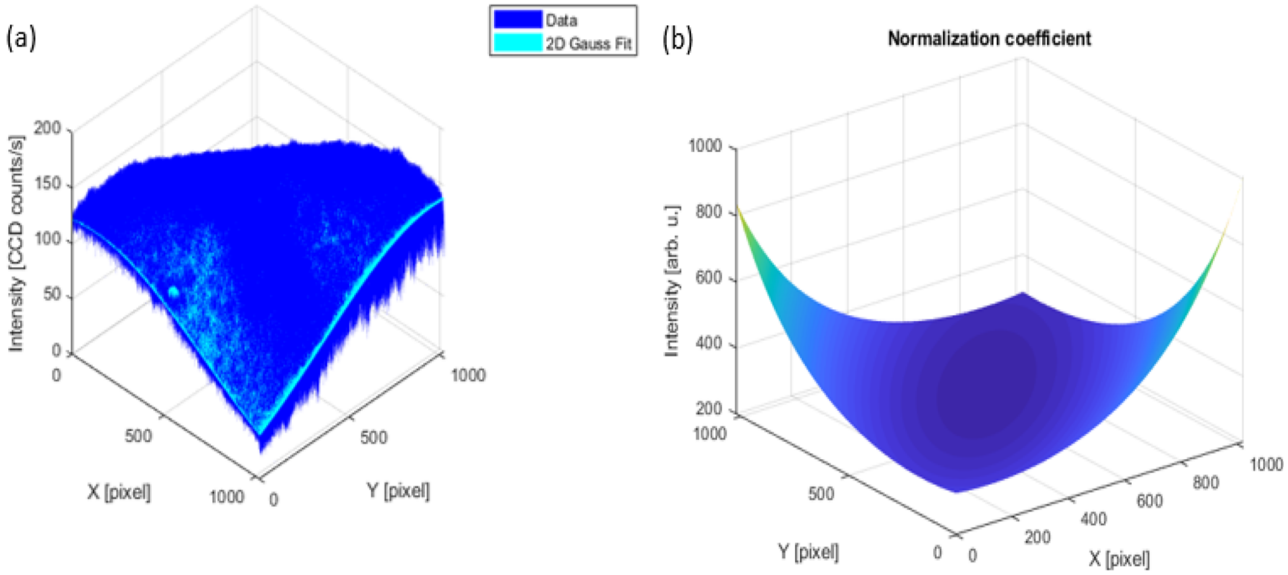

Figure 4.3: (a). Fitting of the excitation spot; (b). Normalization Factor for the image correction.

The second step of the image processing consists of the PL intensity extraction for every single EV. The first selection of the region of interest (ROI), illustrated in *Fig. 4.4(a)*, was performed to identify the area of the image to analyze. It is recommended to select the areas in the center of the image since the focus and the intensity distribution would be more accurate compared to the edges of the image. Once this step was completed, each object was selected by a threshold, as shown in *Fig. 4.4(b)*, and then the respective PL intensity was extracted using a plugin in ImageJ, specifically created for this step. And the end of the analysis, an array with the EVs intensity and the respective coordinates of the EVs in the image is given, that is useful for the following step of the analysis, for the identification and characterization at the single-particle level.

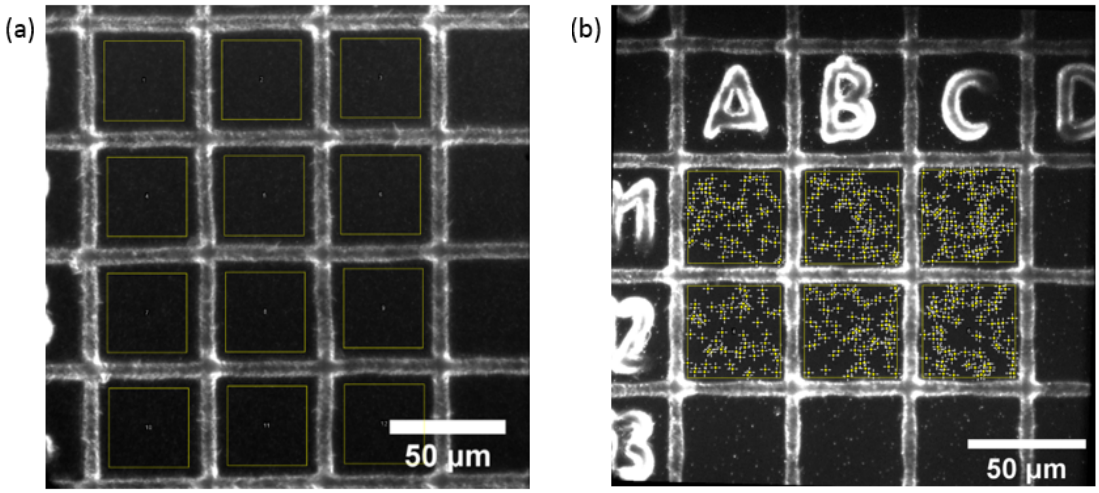

Figure 4.4: (a). n.12 selected region of interests (ROI) represented by the yellow thin frames; (b). PL intensity extraction of diffraction-limited spots, representing single EVs, here marked by yellow crosses inside the regions of interest.

4.2 Atomic force microscopy (AFM) measurements

Atomic force microscopy is a powerful technique that, with a resolution of nanometers, allows to characterize the structure and function of very small and soft samples, such as cells, proteins, and DNA, in physiological conditions [46]. Thanks to the high versatility of the available methods to perform the scanning of the sample, it is possible to select the more suitable approach based on the sample's characteristics, avoiding possible sample distortion and damage. However, their imaging in physiological conditions remains a very challenging task since many parameters must be take in consideration to properly image biological samples, such as the optimization of their fixation on the substrate, control of the possible contamination both on the substrate and in the tip, the selection of the proper cantilever and imaging mode to minimize the damaging, and finally the application of low interaction forces. On this regard, in our study, as it will be shown in the following sections, it was decided to characterize the size of the sEVs in liquid, using as imaging mode the Quantitative Imaging (QI), which is particularly suitable for soft samples since it works with low forces, and it provides for each pixel of the image, quantitative data such as the adhesion and mechanical properties, but also the recorded forces [22]. Based on this consideration, two different sample fixation methods have been investigated in order to understand which one can give the best compromise to perform the imaging of the sEVs in liquid environment. The main parameters that will be taken into consideration are the control of the height distribution after the surface modification, the number of vesicles attached to the substrate, and shape preservation.

4.2.1 Basic principles

Atomic force microscopy belongs to the family of scanning probe microscopy techniques (SPMs) that is formed by three different subclasses: scanning near-field optical microscopy, atomic force microscopy, and scanning ion conductance microscopy [37]. The name of each technique depends

on the interaction that it is measured. Therefore, the AFM measures the attractive and repulsive forces between the surface of a sample and a very sharp μm-sized Si cantilever. The cantilever represents the heart of the system and is a rigid element fixed at one end and free in the opposite end where a sharp tip is mounted [22].

The main detection principle of AFM, illustrated in Fig 4.5, is based on the measurement of the cantilever deflection which depends on the type of interaction (attractive/repulsive) between the tip mounted on its end and the surface of the sample. In particular, the deflection is determined by the tilt angle of a laser beam that is reflected from the reflective side of the AFM lever onto a position-sensitive detector. The bending angle is then converted into deflection. Therefore, the force is obtained multiplying the stiffness of the lever for the probe distance from the sample ($F = -k \cdot z$, where k is the stiffness and z is the distance). Usually, a feedback system maintains the applied force by the tip constant. The value of the force is then converted into an electrical signal that is used to create the AFM image of the surface [22].

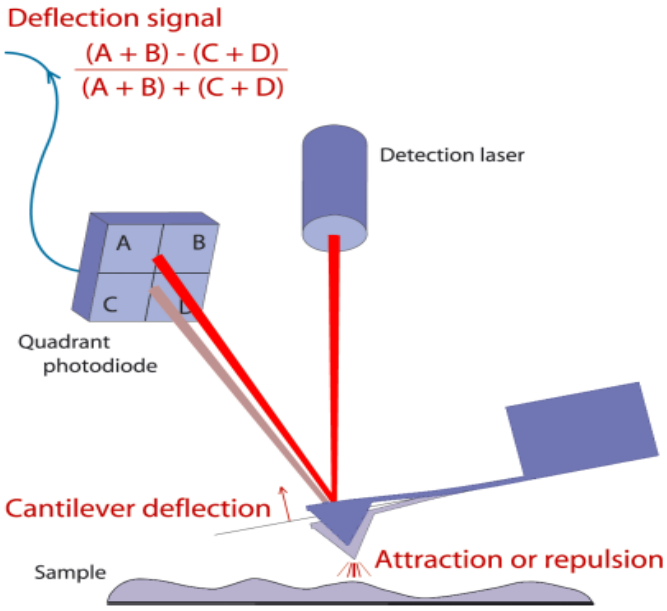

Figure 4.5: AFM basic principle of detection [22].

Since the force applied by the cantilever depends both on the deflection and the constant spring of the cantilever, these two parameters must be optimized depending on the type of the sample. It is possible to modulate the cantilever deflection by changing the imaging mode, whereas for the constant spring it is possible to change the length and material of the tip [15].

Different types of tips differ in material, shape, coating, and length. The conventional tips are made with silicon and the free end is completely coated with a metallic material, commonly with aluminum. Unfortunately, the total coating could affect the mechanical properties of the cantilever. Therefore, new tips with only a short-coated region are increasingly being used, especially for the measurements in a liquid environment where it is more difficult to maintain stable properties. The combined use of a partial coating made with a material characterized by good optical properties such as gold permits at the same time to obtain a better reflectivity and also to reduce the drift and bending of the cantilever [15].

Depending on the choice of a cantilever characterized by certain material and shape, it is possible to perform different imaging modes that can be divided into contact mode, dynamic mode, and rarely non-contact mode. The main differences between these modes and how the force applied to the sample changes during the scanning of the surface and how the cantilever and how the cantilever approaches the surfaces. In contact mode, the force value remains constant since the distance of the cantilever from the surface of the sample is modified for each variation of the surface height. In this way, each point of the surface receives the same applied force and the cantilever remains in contact along the whole analyzed region. For what concerns the dynamic mode the cantilever oscillates along the surface. It is possible to perform this imaging mode in three different ways: intermittent contact mode, non-contact mode, and force modulation mode. However, the most adopted is the intermittent contact mode in which the oscillation amplitude is modulated according to the sample height [22].

As already mentioned, the applied force depends on the spring constant of the cantilever, therefore each imaging mode will require different cantilevers. In the case of contact mode are commonly adopted softer cantilevers with a spring constant value lower than $0.5\,N/m$. Whereas for the intermittent contact mode, the choice of the cantilever varies depending on if the imaging is performed in liquid or in air. For imaging in air are required stiffer cantilevers, while for the imaging in liquid it is possible to use the same cantilevers adopted for contact mode.

4.2.2 Quantitative imaging mode

The imaging mode that has been chosen to characterize the single EVs is the quantitative imaging (QI). This imaging mode can be performed, without losing in resolution, both in air and in a liquid environment. It allows to measure adhesion and to extrapolate size at null force. At the same time, it is possible to control the force applied on the surface. Furthermore, all the calculated force curves are provided and can be used to calculate further parameters [10].

The main mechanism involves the cyclical alternation between one pixel and another, of an approach phase and a complete retraction phase of the cantilever, with the application of low forces. This makes quantitative imaging particularly beneficial for soft samples imaging, such as vesicles, since the lateral forces that could damage or detach them are avoided. The baseline parameters are chosen and optimized automatically by the software, based on the sample and the tip properties that are selected by the user [22]. This allows for constant parameters throughout the acquisition, unlike the other imaging modes in which especially the extend baseline can be critical and it must be manually adjusted. Generally, the driving frequency and the setpoint must be changed once the cantilever has finished the approach. Nevertheless, if the measurement is made in liquid, the choice of the driving frequency can be complicated. For this reason, it can be deduced that the result of a good imaging acquisition is operator-dependent, while this is not required for quantitative imaging. To perform quantitative imaging is recommended to use cantilevers with low spring constant, medium/high resonance frequency and low/medium length, to minimize the noise and perform fast measurements. Since the EVs are extremely soft, it is better to use low forces and try to have a short interaction between the sample and the tip to reduce the drift of the sample [22].

4.2.3 AFM setup

The adopted system configuration, illustrated in *Fig. 4.6*, is composed of the life science stage which is specifically used with the inverted optical microscope, to perform combined analysis with the two tools; on top of the system is mounted the ZEISS AxioCam MRc that is used to align the selected tip with the center of the $100x\,oil$ immersion objective; then we have the AFM head which represents the main component of the system, formed by three different stepper motors and z piezo located in the cantilever holder. These two elements are moved alternately so that the cantilever can reach the surface, moving along the z-axis. Before starting the approach phase, the laser must first be aligned with the tip and then the cantilever must be calibrated. In QI this last step is performed by the software. Once these steps are done, it is possible to start the scanning of the surface. To perform our measurement, it was decided to take images of $5 \times 5\,nm$ with the image resolution set at 512×512 pixels.

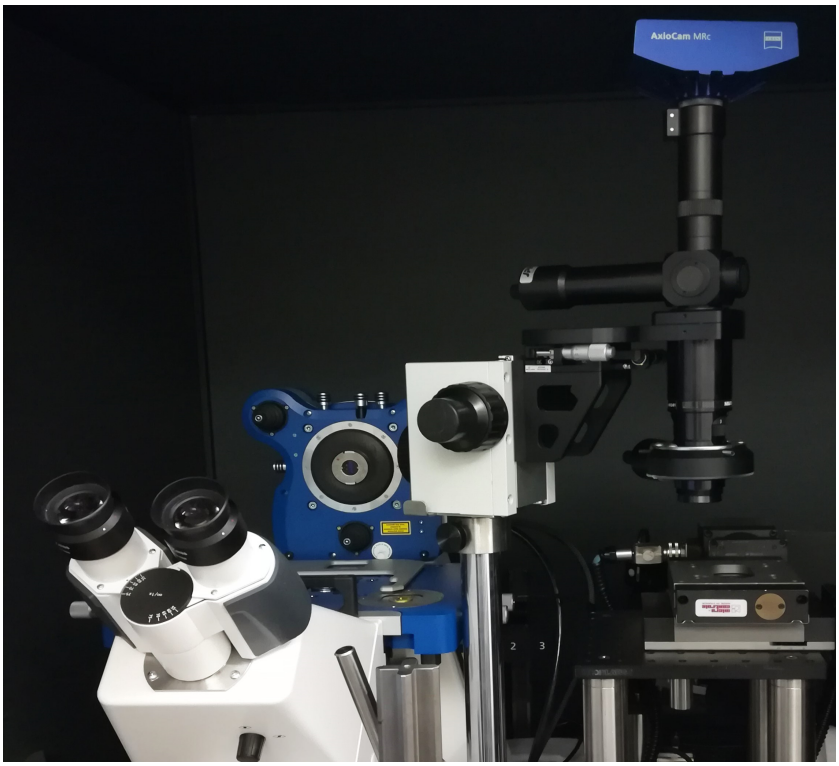

Figure 4.6: System configuration for combined AFM-PL measurements.

To perform the QI measurements, the sample was first fixed on a glass disk, as described in chapter two, and subsequently, several washes were performed to eliminate residual impurities and remove the vesicles not attached to the substrate. After that, once the sample holder was placed in the life science stage, it was necessary to deposit a droplet of $10\,\mu L$ of 1×PBS on the free end of the probe, to break the surface tension between the tip and the liquid during the immersion of the cantilever into the liquid. This step is critical since care must be taken to avoid the contamination and damaging of the tip. Once the probe was immersed in the liquid, the following parameters

have been set as:

- Temperature: $23^\circ C$
- Medium: $1XPBS$ ($Density = 1.005\, kkg/m^3$ and $Viscosity = 1.05\, mPa \cdot s$)
- Ashesion: medium
- Expected Height: $100\, nm$ for the control surface with only GA, $300\, nm$ for the surface with GA and EVs on top

The cantilever used to perform single EVs imaging were NANOSENSORS qp-BioAC probes designed for imaging in air and liquid. These probes are characterized by the presence of three rectangular cantilevers with different lengths and consequently with a different resonance frequency and force constant. They differ from traditional cantilevers since they are made of quartz-like material and have a partial gold coating. Thanks to their uniform thickness ($370 \div 430\, nm$) the resonance frequency and the dispersion of the force constant are minimized since their value is directly proportional to the thickness of the cantilever. For our measurements, it was chosen the central tip (NANOSENSORS qp-BioAC-CB2 AFM probe) since it has the resonance frequency in the range of $35 \div 65\, kHz$, the force constant in the range of $0.06 \div 0.18\, N/m$, and medium length between $55 \div 65\, \mu m$.

4.2.4 AFM imaging (processing and analysis)

The following data processing and analysis have been applied to all the acquired AFM height images. All the steps that will be described below, have been carried out with Gwyddion software.
The first step of the image processing consists of the alignment of the lines of the image which may be evident in case of a fast scanning of the surface. Correction can be carried out using various methods including the median method adopted by us. For each line of the scan, this method subtracts the respective average value of the height of the line itself. The horizontal scar correction is then applied to remove the scanning errors of the image. Thereafter, each single EVs is selected by applying a mask with the command 'mark grains by threshold' which allows identifying all the EVs with the height above the set threshold. To discriminate between the surface and the EVs, a height value of 10nm was chosen, since we do not expect to have EVs below this value and it has also been observed that the surface without EVs presents heights in the order of $4 \div 10\, nm$. In the last step, the surface is leveled using a first-degree polynomial subtraction, with the exclusion of the mask region.

For the data analysis, the distributions of the heights and radius were exported for each image. In addition, the height, the equivalent disc radius, and the surface area were extrapolated for each vesicle that had been identified as a single EV by overlapping the AFM image with the PL image.

4.2.5 Correlation between AFM and PL images

The centerpiece of the thesis work is to measure the correlation between the information obtained from the photoluminescence measurements and the measurements obtained with the AFM. As emerged in the second chapter, using only one method of characterization, although this allows for high-resolution measurements, it is not possible to discern with certainty between single small vesicles and clusters of small vesicles or other particles in the range of small EVs due to the diffraction

limit in fluorescence.

In this study, we tried to overcome scientific limits, related to the most widespread approaches that are followed in the characterization of small single vesicles. This was possible thanks to the combined use of the AFM and the PL system which allow obtaining information about the size and expression level of single EVs, thus overcoming the diffraction limit. The AFM was mounted above the sample, instead, the inverted microscope was located below the sample. This allowed to analyze the same area of the sample with the two different methods. The results obtained from the measurements were first analyzed individually and then they were combined by overlapping the images obtained with AFM and uPL setup.

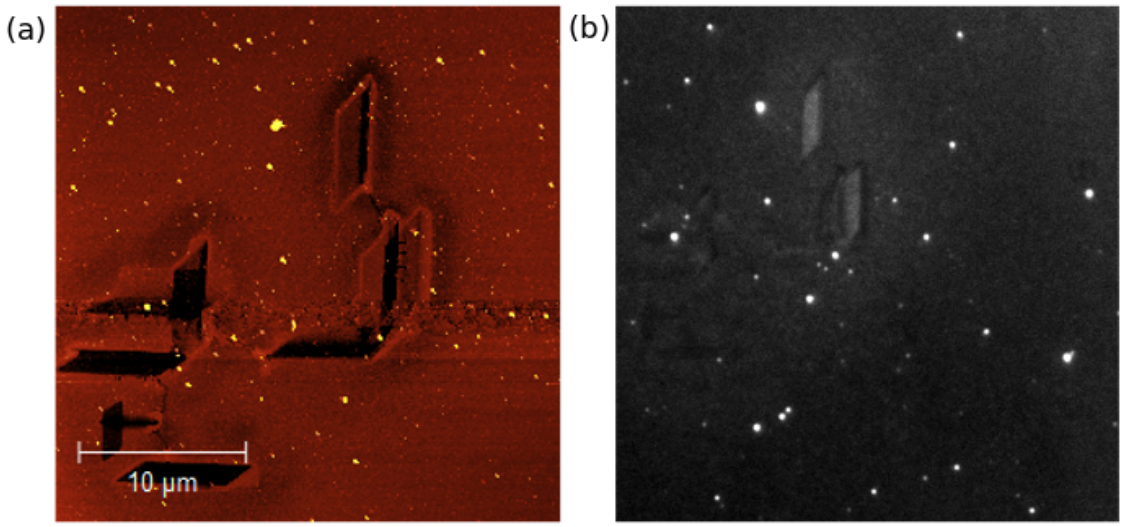

Figure 4.7: (a) AFM and (b) PL - image of the patterns etched in the glass substrate.

To exactly realize the alignment between the PL image with the AFM images, different patterns have been created along the surface of the glass slide using the FIB-SEM technique. To make the overlap, it was first necessary to take the fluorescence image in order to select the patterns that were more visible and at the same time located in an area with a good number of vesicles. As it can be seen from the *Fig.4.7(b)*, on the right of the PL image there are two clearly visible patterns, instead on the left there are other patterns that are difficult to identify since they are characterized by a gray level similar to that of the image background. This difference is due to the depth of the markers realized with the FIB-SEM etching that unfortunately is not well reproducible. Moreover, it can be seen that in the area around the mark, the substrate is different and the number of sEVs was lower compared to the other areas. Hence, since these aspects are mainly related to the etching steps of the surface, by first imaging the substrate with the fluorescence microscopy, it is possible to quickly visualize which areas have the best features for proper imaging of the vesicles and to perform an accurate overlap with well visible patterns. After that, a first scan of an area of $30 \times 30\,\mu m$, was made to visualize the patterns in the AFM height image too, as shown in *Fig. 4.7(a)*. Starting from this image, the PL image was imported into the AFM software to realize the overlap of the patterns, that allows identifying which areas of the surface that have EVs in PL image, must be analyzed with the AFM. Afterward, multiple high-resolution scans were realized in

the selected areas for the size characterization of the single vesicles. In particular, were considered as single vesicles those identified from the overlapping of the two images, thus they were present as isolated spots in both images. For those, the PL intensity was extracted from the PL image while the size was measured from the AFM image. An example of how the overlap was performed will be illustrated in the next chapter.

Chapter 5

Results and Discussion

5.1 Characterization of single sEVs by PL

5.1.1 Preliminary sample characterizations

This section will show the preliminary characterizations that have been carried out to choose which sample was better to use for the validation of the protocol, which type of surface functionalization has been adopted and the parameters to optimize.

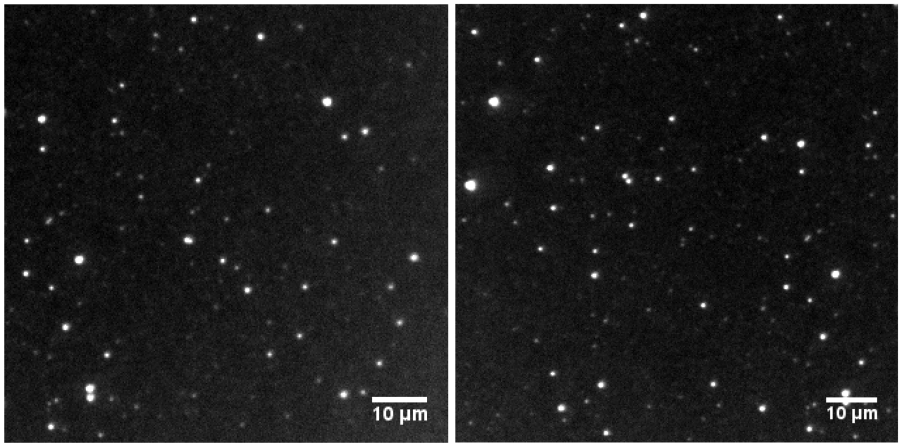

Figure 5.1: Photoluminescence images of sEVs derived from the engineered cell line HEK293 - fixed on GA. The bright diffraction-limited spots correspond to single or multiple sEVs.

The *Figure 5.1* shows the photoluminescence images of the small vesicles derived from the bio-engineered cell line HEK293, transfected to overexpress the CD63 protein labeled with mNeonGreen. To analyze the results only the central area of the image was taken into consideration since it is the one with the best focus and given that the background is less uniform at the edges (i.e. more uncertainty in the PL intensity values could be introduced if the edges were considered as well). *Figure 5.1* shows the presence of bright diffraction-limited spots that correspond to single or multiple sEVs, uniformly distributed in the substrate, having different intensity. This is mainly related to the different expression levels of the surface proteins of each sEV but also the transfec-

tion efficiency of CD63 tagged with mNeonGreen into HEK293. For higher expression levels, the single EVs will appear brighter, instead for low levels of CD63, the sEV it could be weaker or not detectable. Moreover, the vesicles that are very close or agglomerated, will appear as a single very bright spot.

The same sample was also analyzed with scanning electron microscopy (SEM), a technique that allows obtaining images with a resolution better than 1 nm by scanning the sample with a focused electron beam. However, in that case, the EVs were not in their physiological solution (1xPBS) but were covalently immobilized onto a Si wafer through APTES and GA linker and then sputtered with Au/Pd before imaging to avoid charging of the surface which can lead to image artifacts and lower resolutions. As can be seen from the *Fig. 5.2*, the sEVs seem to have a spherical shape and a diameter of $100 \div 200\,nm$. Furthermore, it is possible to discriminate, with a spatial resolution below $1\,nm$, the presence of agglomerates or single sEVs, which is not possible to achieve with photoluminescence measurements.

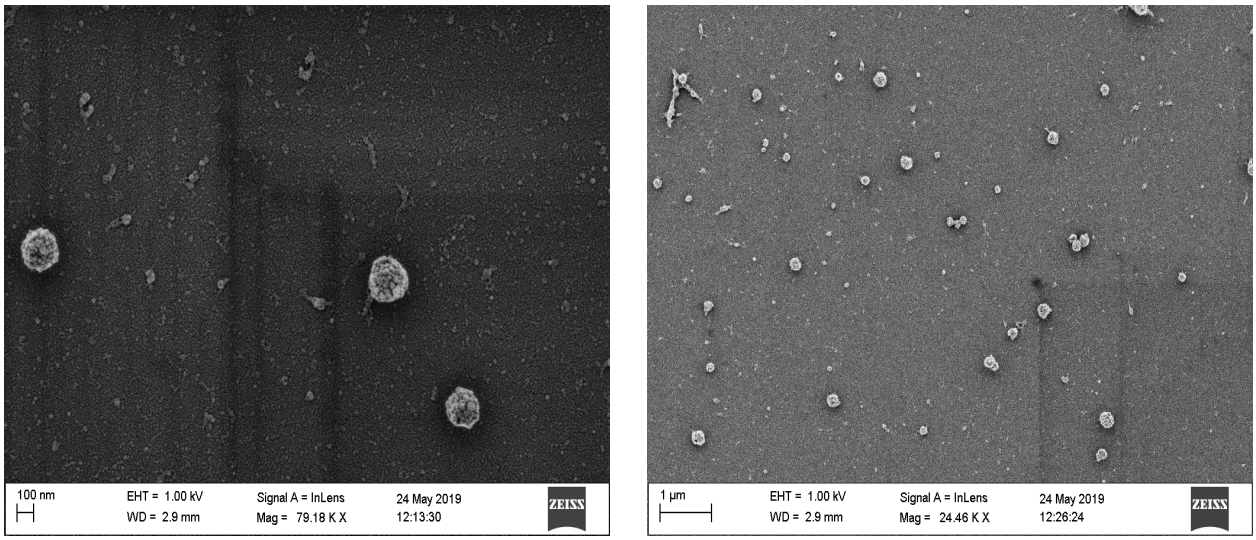

Figure 5.2: SEM-images of sEVs derived from the HEK293 cell line: images were taken using Inlens detector and a voltage of 1kV.

The concentration rate from uPL measurements was then estimated for sEVs derived from the HEK293 cell line, as shown in *Fig. 5.3*. The as found concentration is less than one order of magnitude lower from the one estimated by NTA, which is conventionally used in this case for EVs. In particular, the concentration from uPL is only a factor of ~ 3 lower than NTA and this can be explained by the transfection efficiency of the EVs which should be around 1:3 [11].

Furthermore, it must be taken into consideration that the calculated number of vesicles depends on the selected intensity threshold that is chosen for the vesicle selection. Therefore, all the particles that are still attached to the substrate but are characterized by a fluorescence intensity lower than the threshold (e.g. due to low protein expression level or not successful transfection) will not be included in the total count of vesicles. This means that the real number of vesicles is certainly higher and closer to the number of particles revealed by NTA.
This is not as true for the surface modification with antibodies instead of covalent binding using

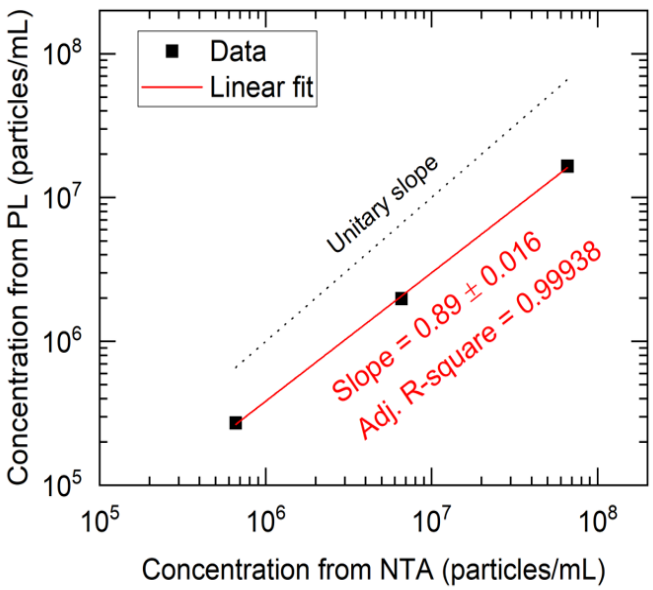

Figure 5.3: Concentration estimated from PL measurements versus the one measured by NTA (black squares). The dotted line is a unitary slope whereas the red line is a linear fit of the data.

APTES and GA since the binding mediated by the antibody it is more specific and a less number of vesicle will be captured. Once we can count the sEVs from uPL we want to check if these are attached well to the substrate. Indeed, the same number of EVs must be present on the surface if, for example, we wash the sample several times with different types of solvent (which is the case in our essay).

Figure 5.4 shows that the number of particles does not change with the increasing number of washing cycles realized with solutions like DIW and ethanol. On the other hand, by realizing serial washing with 1× PBS, it is possible to see a small positive variation of the number of the particles due to the additional binding to the surface of those vesicles that remained in suspension in the previous steps.

These results are related to the glass surface modification that was adopted. In particular, the exposition of CHO groups by GA enables the covalent binding with the NH_2 groups of sEVs. Since the covalent bond is one of the most strong chemical bond, the detachment rate of the vesicles from the surface it is limited. Moreover, it was observed that after 4 hours of measurements with combined AFM-uPL, the number of vesicles remained almost unchanged. This may not occur in case of surface functionalization with antibodies since their capture is more specific compared to GA in which all the sEVs in the solution can remain attached. Hence, the number of captured vesicles remains lower.

To conclude, comparing our results obtained with those provided by the other studies available in the literature, it has been observed that with our single sEV assay it is possible to achieve a capture efficiency equal to $20 \div 30\,\%$ compared to the average capture rate per vesicle of $4 \div 10\,\%$ that is normally achieved in other single EV studies [25].

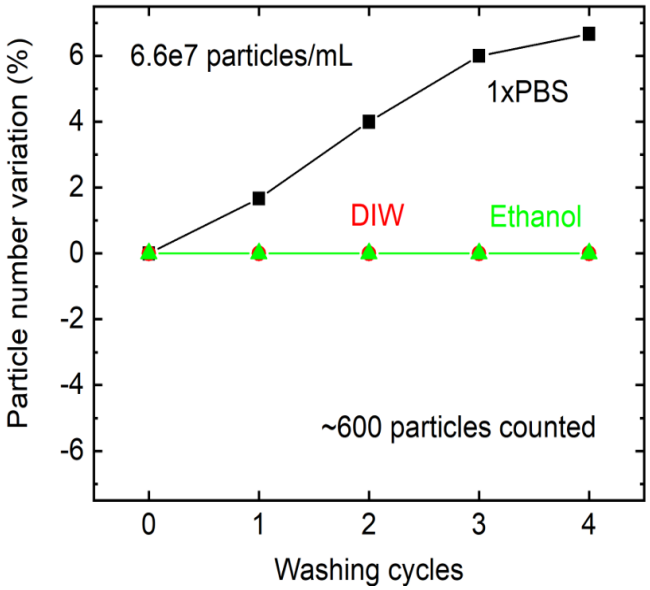

Figure 5.4: Particle number variation as a function of the washing cycles, for three different materials: DIW, ethanol and 1x PBS.

5.1.2 Evaluation of CD63 and CD9 expression level

In this section, the surface molecular profiling of CD63 and CD9 proteins is described. We decided to investigate these two tetraspanin proteins because they are considered important biomarkers of sEVs, due to their pivotal role in the vesicle formation and tumorigenesis processes [4].

The study is based on the measurement of the fluorescence intensity by two different fluorophores, mNeonGreen and Alexa Fluor 647, which respectively require two different excitation sources: blu-LED ($\lambda = 455\,nm$ at $0.56\,mW$) and red laser ($\lambda = 632\,nm$ at $5\,mW$). The mNeonGreen was used to profile the expression level of CD63 since the cell line HEK293 was transfected with CD63-mNeonGFP tagged to over-express the CD63 protein, while the expression level of CD9 was investigated by performing the CD9 labeling with CD9-Ab conjugated with AlexaFluor 647 and using a red-laser as excitation sources. The red laser has only been used in preliminary tests to verify the effectiveness of the analysis method while the blu-LED was also used for the subsequent characterization of the chosen sample and the combined analysis with the AFM.

The first characterization test aims to analyze the expression level of CD9 and CD63 on sEVs derived from the cell line HEK293 transfected to overexpress the CD63 tagged with mNeonGFP. In that case, the vesicles were first immobilized onto a glass slide through APTES and GA linker with their subsequent coupling of CD9-antibody conjugated with AF647 on top of the sEVs. In particular, all the functionalization steps were performed on the glass slide in combination with a rubber-well formed by 4 wells, each of $110\,\mu l$ capacity. After the functionalization, the EVs were inserted in only n. 2 wells, whereas the others were kept as a control and contained 1x PBS. Different areas, approximately $100 \times 100\ \mu m^2$ each, were probed inside every well. Two PL images

were taken per area: one "green" (emission max at 506 nm) and the other "red" (emission max at 695 nm). For the former excitation channel, the signal was filtered with a GFP filter cube, for the latter it was used a long-pass filter at 650 nm.

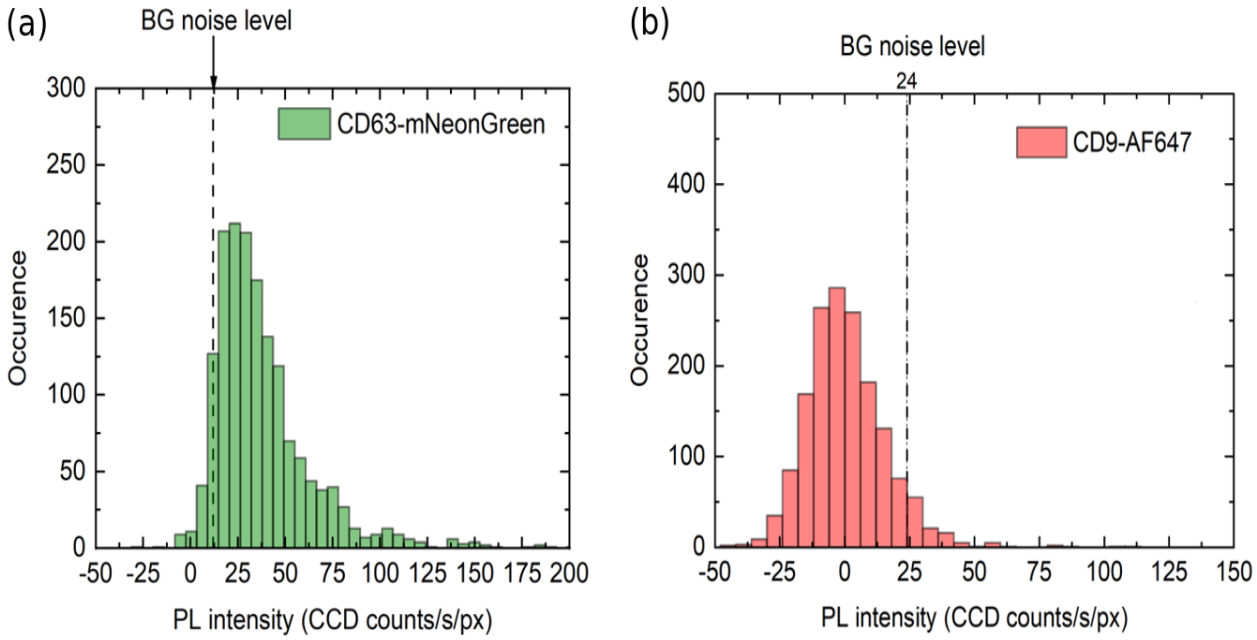

Figure 5.5: (a) Photoluminescence intensity distribution of CD63-mNeonGreen. (b) Photoluminescence intensity distribution of CD9-AF647.

Figure 5.5(a) shows the distribution of the photoluminescence integrated intensity related to the CD63 protein. To correctly interpret the graph it must be taken into account that as background noise level it was considered the standard deviation of the mean PL intensity of the control and the plotted intensities values are obtained by subtracting the background value from the intensity of each vesicle selected by a threshold. The same considerations are valid for the *Fig. 5.5(b)* in which it is possible to observe the photoluminescence integrated intensity distribution of the CD9 conjugated with AF647. As expected, in *Fig. 5.5(a)* the majority of the signal is above the background noise level since these vesicles are modified to over-express the fluorescent CD63 protein. Instead, in *Fig. 5.5(b)* there is almost no signal. Theoretically, the CD9 should be $3 \div 10$ times less expressed than CD63 hence the obtained results could be considered reasonable, but since at the beginning we can not be sure if the absence of the signal was related to the unsuccessful binding of the antibodies to the EVs or the low expression level of CD9 in the cell line HEK293, two more tests were carried out.

One test aims to prove the bonding effectiveness of the antibodies, the second one involves a different cell line to solve the doubt related to the expression level of CD9. In this way, we can prove if our single EVs assay works or not, and also, we can decide which sample it is better to use for subsequent characterizations.

The first test aims to verify the antibodies capture efficiency by functionalizing the surface with

CD9 antibodies instead of GA and using two different samples, the sEVs from the cell line HEK293 and the sEVs from the cell line H1975. The first one overexpressed the CD63 protein against the low expression level of CD9, the second one is characterized by equal expression of CD63 and CD9. *Figure 5.6* shows the PL images of single sEVs derived from the cell line HEK293 (left) and H1975 (right), fixed onto a glass slide through APTES, GA and CD9-Antibodies.

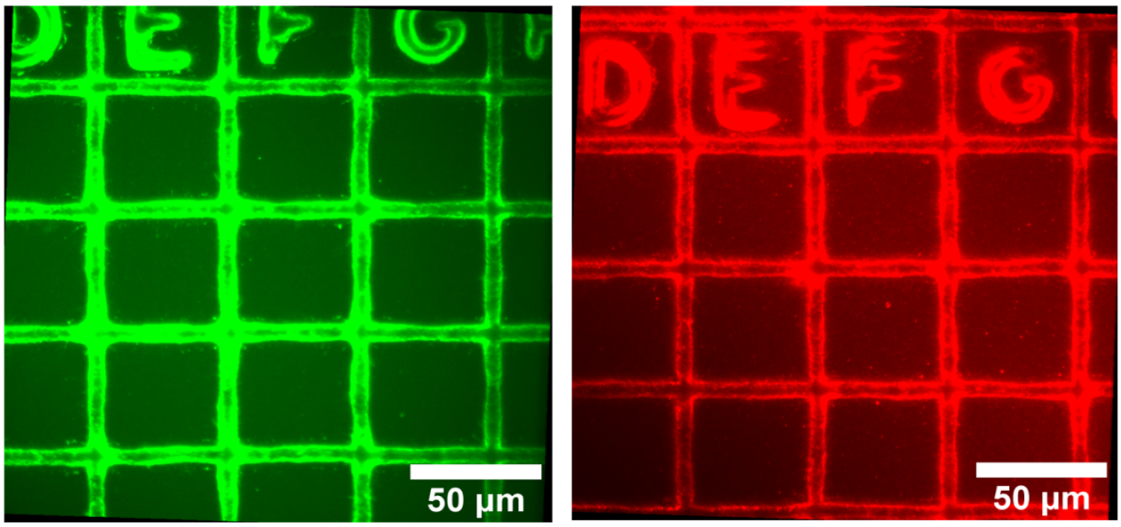

Figure 5.6: PL image of - (left) sEVs from cell line HEK293 on CD9-Antibodies and (right) sEVs from cell line H1975 - on CD9-Antibodies.

It was observed, as expected, that the number of sEVs captured by antibodies was lower compared to GA since the bond mediated by antibodies is more specific and directly depends on the expression level of the vesicles. For GA this is not valid because it mediates a non-specific covalent binding of the majority of vesicles present in solution. Furthermore, in that specific case, the number of captured sEVs was even lower for the cell line HEK293 compared to the cell line H1975, due to the low expression level of CD9.

For these reasons, we decided to investigate the sEVs derived from lung cancer cell line H1975 which presents an equal expression of CD63 and GFP-tagged CD9. The presence of GFP allows profiling the expression level of CD9 using a blu-LED excitation instead of a red-laser as in the previous experiment shown in *Fig. 5.5(b)*. This was a great advantage since the image acquisition with the red-laser could be more critical in terms of the focus of single EVs and the photoluminescence intensities of AF647 are generally weaker compared to the GFP. This second test aims to profile properly the CD9 expression level of sEVs from the cell line HEK1975, and wants to support the results obtained from the previous one in terms of antibodies capture efficiency.

Figure 5.7 shows the PL image of the sEVs derived from lung cancer cell line H1975 containing the tetraspanin proteins CD63 and GFPtagged-CD9. The sample was first immobilized onto a glass slide through APTES and GA, with their subsequent coupling of CD9-antibody conjugated with AF647. It can thus be possible to have a double-check of the sEVs expression level of CD9 by exciting the CD9 protein with both the blu-LED and the red-laser. The second excitation channel

also gives information about the antibody binding.

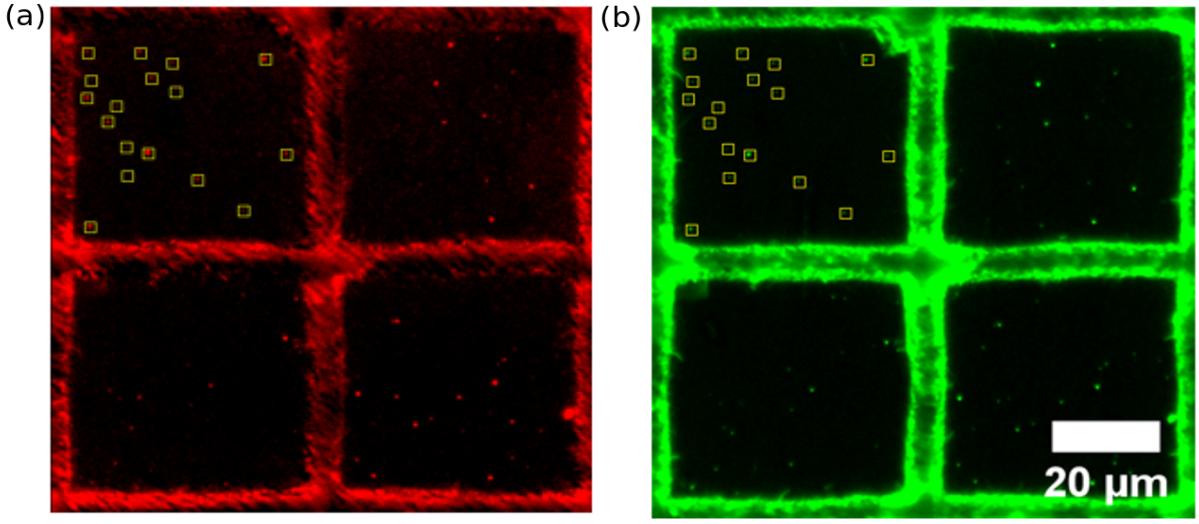

Figure 5.7: PL images of sEVs from cell line H1975 fixed on GA and labeled with CD9-Ab conjugated with AlexaFluor 647. (a) Red laser excitation of CD9-Ab conjugated with AF647; (b) Blu-LED excitation of GFP-tagged CD9.

Fig. 5.7 above shows that the same number and position of vesicles is present in both *Fig. 5.7(a)* and *Fig. 5.7(b)*. This allowed us to conclude that: first, the vesicles derived from the cell line H1975 express the CD9 protein, as they are visible in the *Fig. 5.7(b)*, which was taken with the blu-LED for the excitation of the GFP-tagged CD9; second, the binding of the antibodies was successful, as the same number of vesicles is visible in the *Fig. 5.7(a)*, taken with the red laser for the excitation of the CD9-antibody conjugated with AF647.
In support of these considerations, *Figure 5.8* shows the photoluminescence intensity distribution related to the GFP-tagged CD9 (*Figure 5.8(a)*) and CD9 conjugated with AFL47 (*Figure 5.8(b)*). Comparing these results with the ones illustrated in *Figure 5.5*, the presence of a positive signal in both excitation channels is now clearly visible. As can be seen, the occurrence of high intensities is greater in the green channel than in the red one, and this could be related either to the maximum emission of the targeting-agent or to the quality of the acquired image. In general, it was observed that the signal from the red-laser excitation was weaker.

In conclusion, these preliminary tests aimed to characterize the expression level of two tetraspanin family proteins, CD9 and CD63, that are reported to be expressed in the cell line HEK293 from human embryonic kidney and H1975 from human lung cancer. Their main difference is that the first sample is characterized by the overexpression of the CD63 tagged with mNeonGFP, the second sample instead has an equal expression of both proteins with the CD9 tagged with GFP. We have seen that with our single sEVs assay, it is possible to profile at least two biomarkers per time, by using two different excitation sources, in that case, the blu-LED was used to excite the green fluorescent protein, and the red laser was used to excite the fluorescent dye AF647. By comparing the results of three different tests it was determined that the sEVs derived from the HEK293 cell line are characterized by a low expression level of CD9 that is probably affected by the transfection

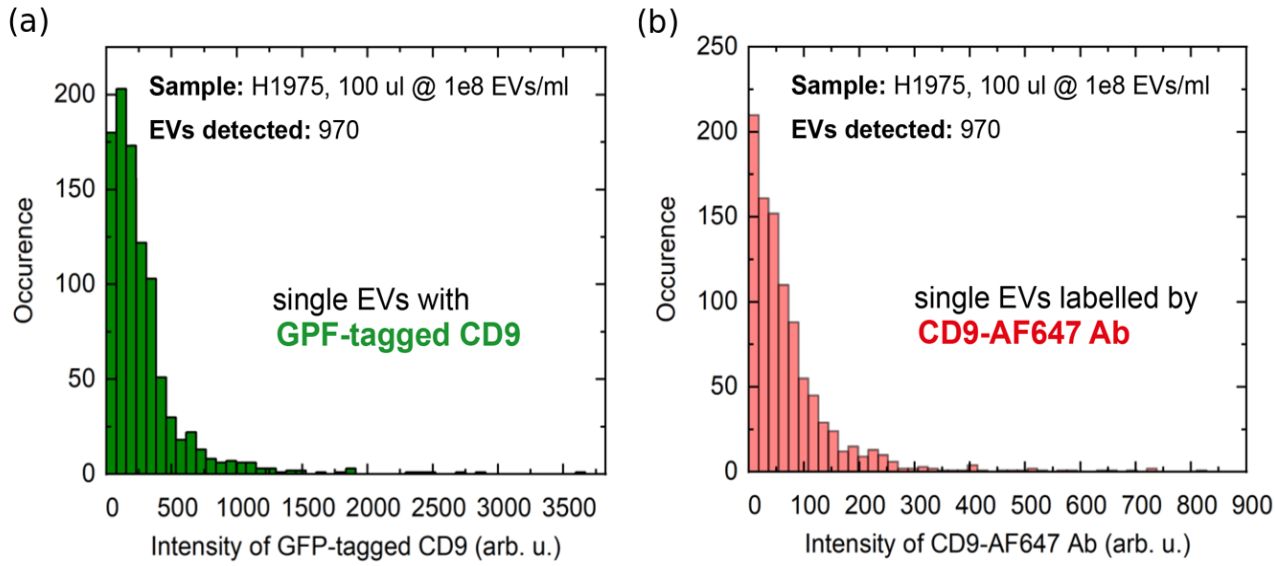

Figure 5.8: Photoluminescence intensity distribution of - (a) GFP-tagged CD9 and (b) CD9-AF647 - of sEVs derived from H1975 cell line.

processes, whereas the EVs derived from H1975 cell line show, as expected, a similar expression level of CD63 and CD9. For these profiling test, two different functionalization processes were analyzed, one with the sEVs fixed on GA and one with the sEVs attached on Ab, and it has been observed that in the second case, the number of vesicles attached to the substrate was always lower since the capture of the vesicles is strongly limited by the expression level of the target protein.

Based on these results, it was decided to continue the characterization of single sEVs derived from the cell line HEK293, since they can be easily immobilized on GA without the need of antibody binding, and they also show a high signal of CD63 protein that can be detected using the blu-LED excitation, without any problem related to the laser alignment and additional step of labeled-antibodies binding on top of the sEVs.

5.2 Characterization of single sEVs by AFM

The second step of the sEVs analysis aims to characterize the size of sEVs in a liquid environment by performing Atomic Force Microscopy measurements. The measurements were done in liquid since we want to reflect as much as possible the native environment of the vesicles. However, the measurements in liquid could be more complex compared to the measurement in air, due to the additional steps that must be carried out to perform the measurements, as well as the challenge imposed by such measurements [22]. It is indeed required the immobilization of the vesicles onto the substrate through a functionalization procedure, which in turn could introduce impurities and increase the roughness of the surface. Besides, the time factor must be taken into consideration as all the steps needed to analyze the sample in liquid required a couple of hours and the actual

measurement generally requires from a minimum of 10 min to 30 min per scan. Nevertheless, the imaging in liquid allows preserving the globular shape of the vesicle as ideally they are kept in conditions similar to those of origin. Furthermore, the drying process that is required in air measurements might affect the morphology of the vesicles, with possible shrinking and size deformation of the particles. Commonly is observed that their height decrease after the drying and they appear more flattened, with the increase of their footprint area [40].

Before proceeding with the size characterization of the vesicles, two different types of functionalizations were compared. In the first method, the surface was first cleaned with the TL1 cleaning and sequentially activated with APTES and GA, whereas, the second method involves the antibodies immobilization instead of GA, and the subsequent blocking steps made with triETHA and casein. The comparison between the two methods was fundamental because the height distribution of the surface increase for each additional step, and it is really important to minimize that increment to clearly identify the sEVs. Since the height of the small vesicles varies from $15\,nm$ to $150\,nm$, the surface roughness should not be greater than $10 \div 15\,nm$.

Figure 5.9 illustrates the height measured with the AFM, of the substrate treated with APTES and GA. The scan of the surface was performed in QI mode in different areas of $5 \times 5\,\mu m$ of the substrate, with a resolution of 512×512 pixel. From the image it can be seen that the substrate is almost flat with the roughness between $0 \div 4\,nm$ and presents some small impurities that arise from the functionalization step.

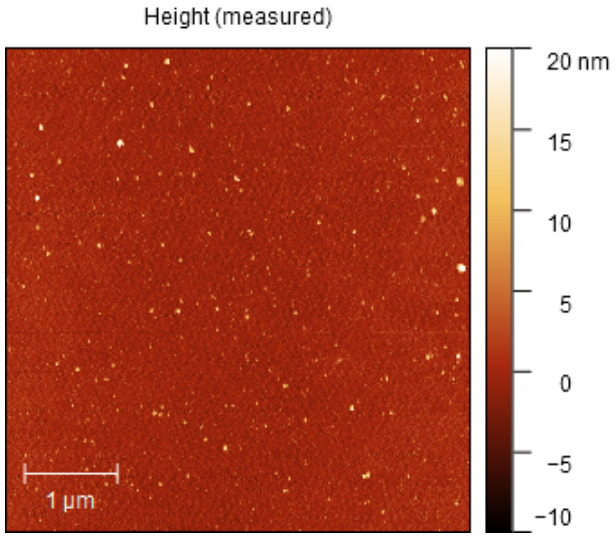

Figure 5.9: AFM height measured image of surface with APTES and GA.

The distribution of the maximum height measured, normalized for the maximum value of the counts, is shown in *Fig. 5.10*. The height distribution starts from a minimum height of $10\,nm$ that was selected as a threshold above which only the small extracellular vesicles should be present. It is possible to observe that the majority of heights vary between $10 \div 12\,nm$, and above $15\,nm$ there is only a small percentage of the measured heights.
This result is particularly useful for the subsequent characterization of sEVs since the increment

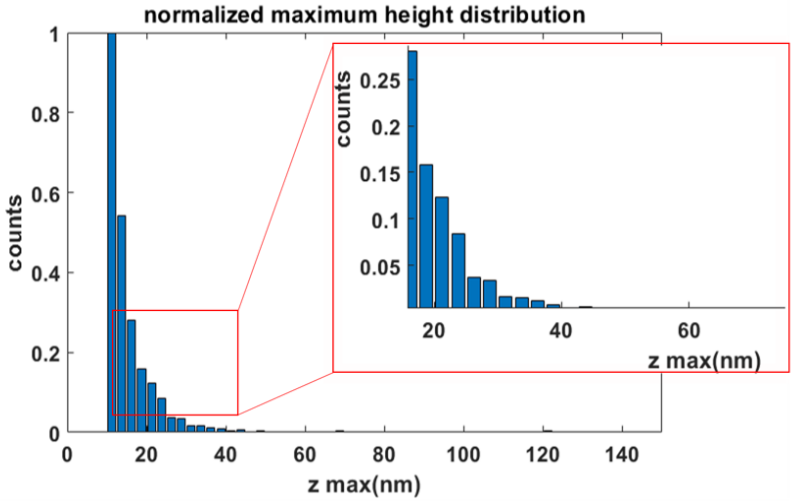

Figure 5.10: Normalized Maximum Height distribution of the substrate modified with APTES and GA.

of the height is not high compared to the initial value of the substrate roughness between 600 pm and 1 nm, calculated after the only cleaning of the slide. If the surface was characterized by a large number of heights above 10 nm, it would not be possible to easily identify small EVs as their size would be in the same range of the roughness.

The same characterization was carried out for the surface activated in sequence with APTES, GA, Antibodies, triETHA, and Casein. It was decided to investigate this method because it mediates more specific binding of the vesicles and we also wanted to see if it can better preserve the globular shape of the vesicles since the region involved in this type of adhesion is smaller compared to the footprint area occupied by the vesicles attached on GA.

Figure 5.11 shows what happens to the surface roughness if we complete a glass functionalization (i.e. up to casein). As can be seen, the AFM height measured of the substrate shows similar results compared to the *Fig. 5.9*. As in the previous test, the substrate is flat and presents a small number of impurities which are identified by the brightest points in the image. The adopted parameters for the acquisition were maintained the same as those used for the previous test.

Figure 5.12 shows the normalized maximum height distribution of the heights above the selected threshold of 10 nm. As it can be observed, the distribution is similar to the previous one shown in the *Fig. 5.10*, with the majority of the counts concentrated in the range of $10 \div 15\,nm$. In that case, the substrate also presents a small number of particles with elevated z max in the range of $30 \div 50\,nm$, which are probably agglomerates of residual impurities or molecules.

It can be concluded that the results obtained by these two tests are relatively similar as they show a quite flat surface, with no significant increment of the roughness compared to the pristine glass slide and a similar distribution of the heights after the functionalization process, in the range

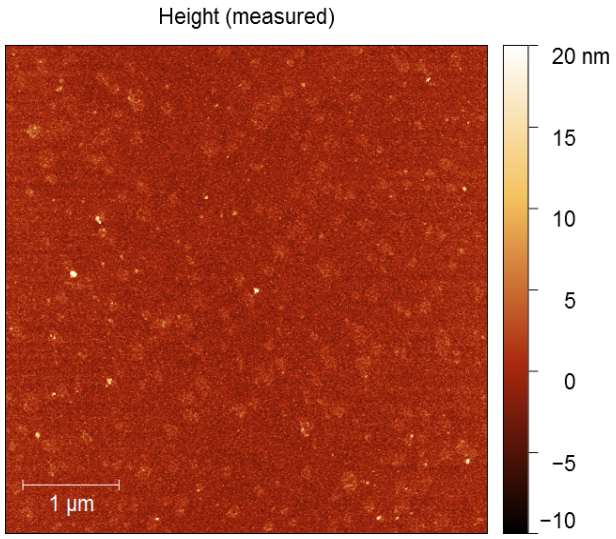

Figure 5.11: AFM height measured image of surface activated with APTES, GA, Antibodies, triETHA, and Casein.

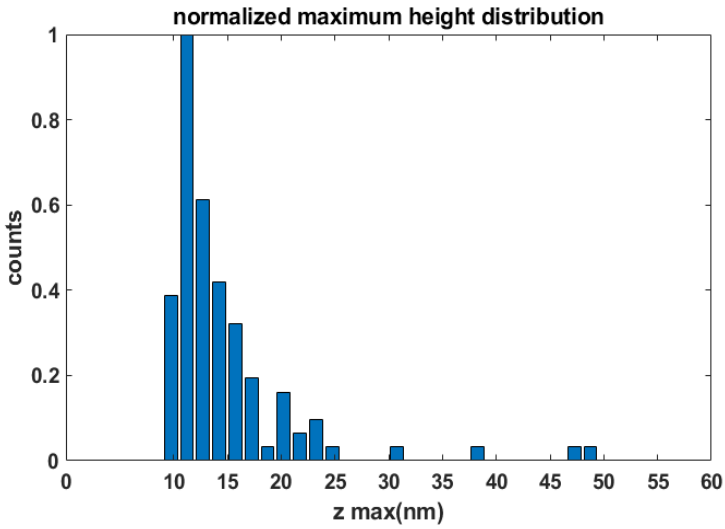

Figure 5.12: Normalized Maximum Height distribution of the substrate modified with APTES, GA, Antibodies, triETHA and Casein.

of interest for the studies that will be shown below.

The second step aims to characterize the height and the radius of the single sEVs by performing the AFM measurements in liquid with QI mode. Although the size distribution of the two different controls was similar, the vesicles were characterized for both types of functionalization, to understand which of the two methods better preserves the globular shape of the vesicles. The surface functionalization with GA allows the capture of more vesicles that remain attached to the surface even after some hours of measurements, but at the same time, due to the strong interaction mediated by the covalent bond between the vesicles and the substrate, the vesicles may be cup-shaped [41],[40]. This phenomenon should theoretically be less accentuated for the sEVs fixation mediated by the antibodies binding since the antigen-binding portion (amino-terminal end of each branch of the molecule) of an antibody is smaller compared to the binding area involved in the vesicles fixation on GA.

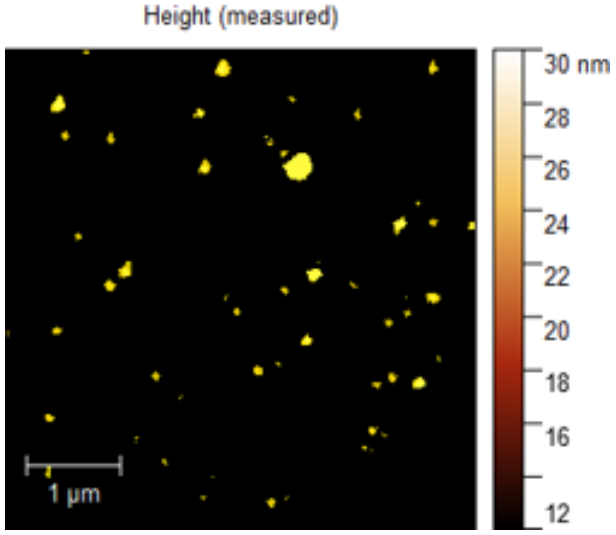

Figure 5.13: AFM Height measured of the sEVs captured on GA - the yellow mask identifies the vesicles with the height above 12 nm.

Figure 5.13 shows the vesicles present on the scanned surface area of $5 \times 5\,\mu m^2$. The vesicles were selected by a threshold of $12\,nm$ since in the previous test it was observed that below this value, the surface does not present a significant number of points. To better recognize the vesicles on the surface it was decided to use a yellow mask for the selected sEVs and a false-color bar that starts with the value of the selected threshold.

Figure 5.14 shows the normalized height (Fig. 5.14(a)) and diameter (5.14(b)) distributions of the identified vesicles. It is possible to observe that the majority of vesicles are characterized by a height that varies between $15\,nm$ to $30\,nm$ and only a small percentage of the vesicles present higher values. Regarding the diameter, the sample was characterized by a homogeneous distribution in the range of $20 \div 160\,nm$ with the highest number of vesicles with a diameter of $20 \div 60\,nm$.
Figure 5.15 illustrates how the height of the sEVs identified as single vesicles, varies as the diameter changes (*more details about the single EVs analysis will be shown later*). It is possible to observe

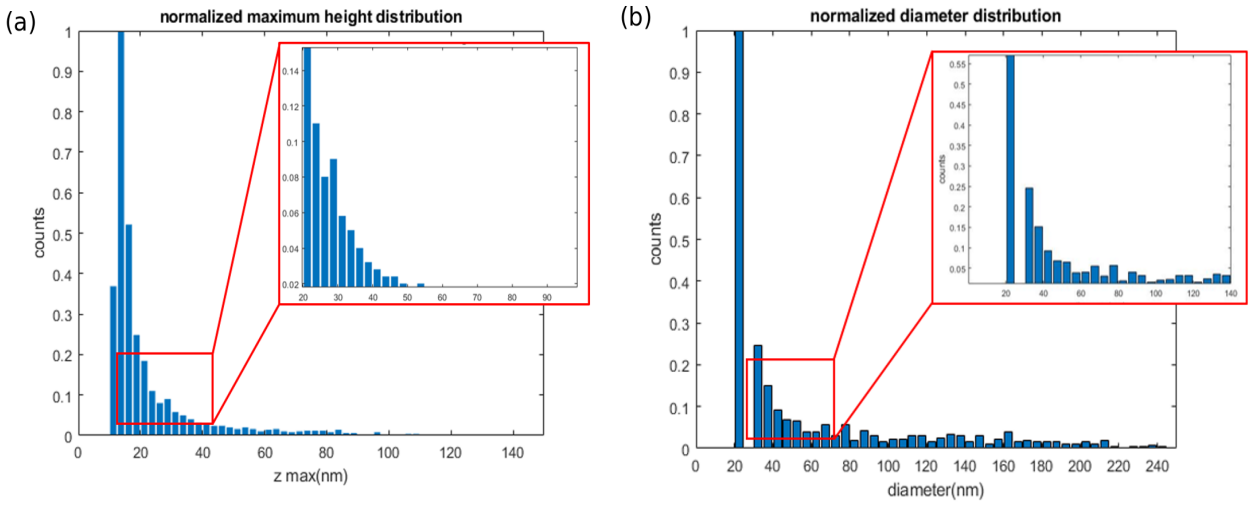

Figure 5.14: (a) Normalized maximum height distribution and (b) Normalized diameter distribution - of sEVs fixed on GA.

that the diameter of the vesicles is much higher compared to the height of the vesicles and it change more slowly compared to the increase of the height. According to these results, as expected, the vesicles seem to be flattened on the substrate. In the graph, there are also some anomalous points, which deviate from the linear trend, and are probably some clusters of multiple sEVs or impurities.

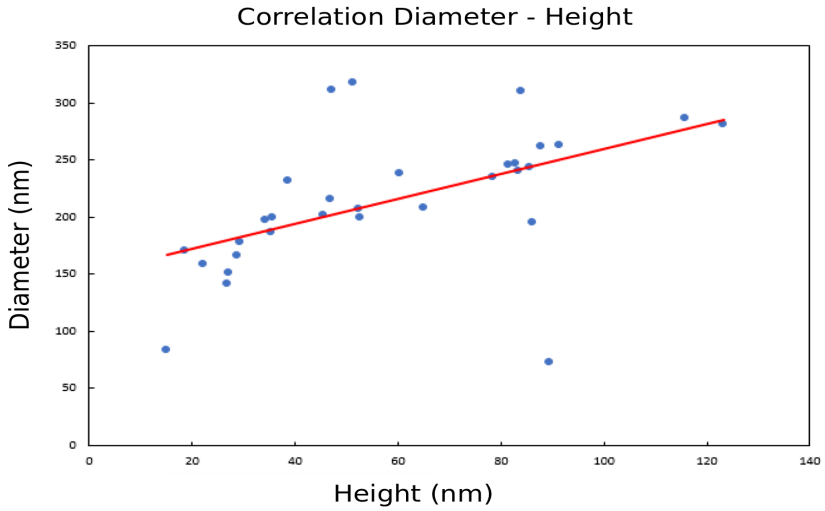

Figure 5.15: Correlation between the Height and Diameter of each vesicles.

Regarding the characterization of the sEVs immobilized on antibodies, the *Fig. 5.16* shows the AFM Height measured of those vesicles with the z size above 12 nm that we decided to consider as a threshold. In order to have comparable data with the previous test, it was decided to maintain the

same parameters and acquisition method. It can be visually observed how the number of vesicles per area is lower than what was observed in *Fig. 5.13*.

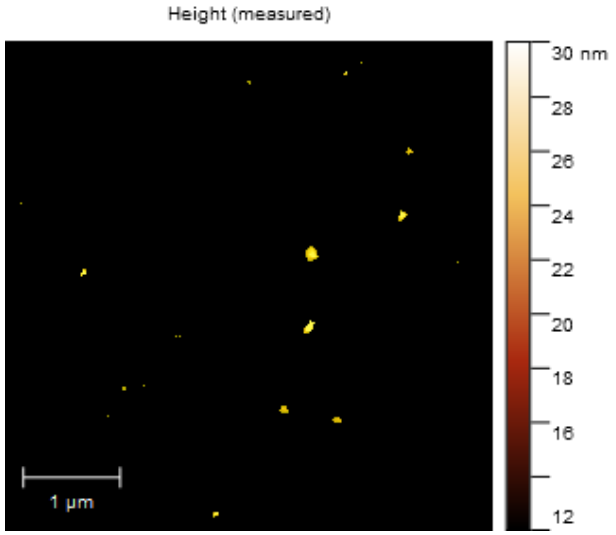

Figure 5.16: AFM Height measured of the sEVs captured on Antibodies - the yellow mask identifies the vesicles with the height above 12nm.

Figure 5.17 illustrates the height and radius distribution of the vesicles attached to the substrate activated with antibodies. As can be seen from the distribution of heights in *Fig. 5.17(a)*, almost all the heights are concentrated in the range of $12 \div 20\,nm$ with only a few vesicles characterized by greater size, in contrast with the previous case were the height distribution was more uniformly distributed in all the z range. A similar distribution has been found for the diameters, as shown in *Fig. 5.17(b)*, that varies in the range of $25 \div 150\,nm$ with a great number of vesicles between $25 \div 80\,nm$ in diameter.

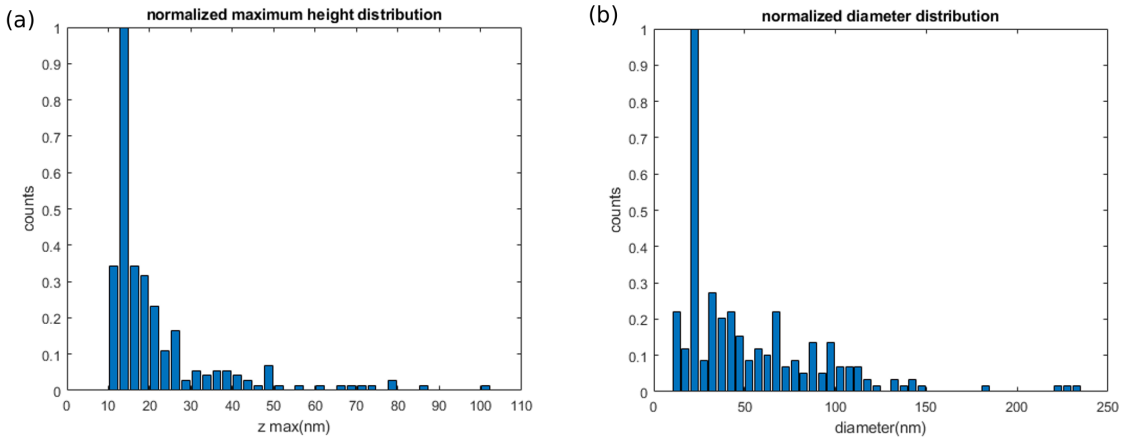

Figure 5.17: (a) Normalized maximum height distribution and (b) Normalized diameter distribution - of sEVs immobilized on Ab.

Figure 5.18 illustrates the correlation between the diameter and the height of those sEVs identified as single vesicles. As expected, the number of single vesicles is lower compared to the analogous test with the vesicles fixed on GA, since the capture mediated by the antibodies is limited to a specific region of the vesicle that the antibody recognizes and binds selectively through its amino-terminal end. Since the interaction between the vesicle and the antibody is non-covalent and so reversible, it can happen that during the scanning of the region of interest, some vesicles can detach and the number of the captured vesicles decreases even more. As in the previous test, by comparing the heights with the respective diameters, it was observed that the variation of the height in function of the diameter follows a linear trend, with the great majority of the single vesicles characterized by height in the range of $12 \div 30\,nm$ and a diameter between $50 \div 150\,nm$, hence the vesicles do not have a globular shape but are flattened, even if this phenomenon is slightly accentuated.

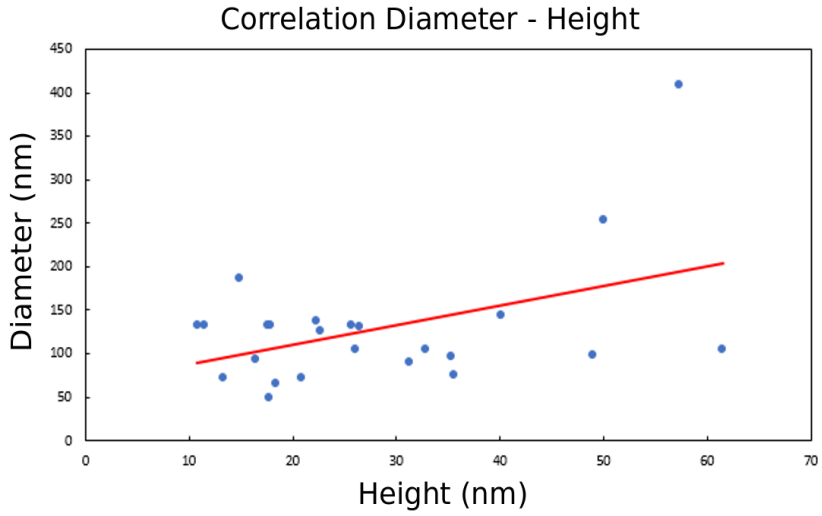

Figure 5.18: Correlation between the Height and Diameter of each vesicles.

By virtue of the obtained results, it was decided to continue the sEVs characterization using the functionalization method based on surface activation with APTES and GA, because no great benefits were observed in the binding of the vesicles with the antibodies, with the only exception of the specific bounding. Apart from that, the time needed for the sample preparation was consistently higher since it requires the three additional steps of antibodies incubation, blocking with triETHA and Casein, for a total amount of three more hours compared to the functionalization based on GA, and at the end of which the globular shape was not better preserved. One other limit is the lower number of particles that can be captured on the activated surface. This aspect is particularly important to obtain significant data which in this case needs to be collected by scanning a consistent number of areas of the substrate, with a consequent extend time for the measurements. On the contrary, by adopting the functionalization with GA, it is possible to perform faster measurements and analyze a larger amount of vesicles, that remain well attached on the substrate during all the imaging acquisition. Since the materials involved in the surface activation are only the APTES and GA, the probability to have impurities is lower compared to the fixation with antibodies, and it also allows to have better control of the surface roughness which is a fundamental requirement

to perform good imaging.

5.3 Correlation between PL and AFM images

The final steps of the sEVs characterization aims to correlate the size and molecular profile measurements of single sEVs, with the two main target of going beyond the scientific limits related to the study of vesicles at the single-particle level, and to help in discovering significative properties highlighted by the correlation of the two measures, that could be important from the biomedical point of view.

The correlation was performed by first taking the PL images in the areas of the sample with both the sEVS and the patterns etched onto the glass disc, needed for the subsequent correlation step. The image was taken using a blu-LED as excitation sources and a 100x oil objective, which can collect more light from the sample compared to the 63x objective that was adopted in the previous characterization steps, thus it was possible to obtain optic images with well defined bright vesicles. After that, the surface was first scanned at a low resolution, with the only purpose of visualizing the patterns identified in the PL image.

Figure 5.19 shows the PL image of the sEVs derived from the cell line HEK293, immobilized on the surface through APTES and GA, where the bright points are the single sEVs or cluster of multiple sEVs, and the marks are illustrated in the yellow magnification of the image.

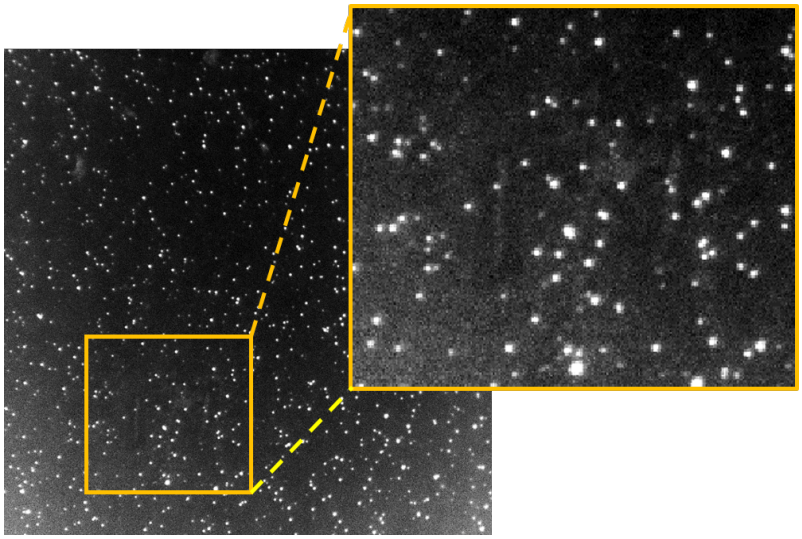

Figure 5.19: PL image of the sEVs derived from the cell line HEK293 - fixed on GA - area with marks.

Unfortunately, as in this case, the marks were not clearly visible, since, even if the input parameters for the realization were $5\,\mu m \times 50\,nm$, the FIB-SEM etching is not well reproducible, and can give in output smaller or bigger patterns. Nevertheless, adjusting the brightness and contrast of the image, it is possible to visualize them. The image was taken using a GFP filter cube since the

vesicles derived from the cell line HEK293 enriched with a CD63-mNeonGFP tagged, with $2\,s$ of acquisition time instead of $10\,s$ of the previous PL tests, to prevent the image saturation.

The respective PL intensity distribution of the EVs is illustrated in *Fig. 5.20*. It is possible to observe that the intensity values in the x-axis are one order of magnitude greater than the results shown before, due to the higher numerical aperture of the 100x oil objective and the different medium between the objective and the specimen, which in the previous PL investigation was the air and in the actual characterization is a droplet of oil deposited above the center of the lens. The illustrated noise threshold of $670\,CCD\,counts/s/px$ was chosen considering 1/3 of the stan-

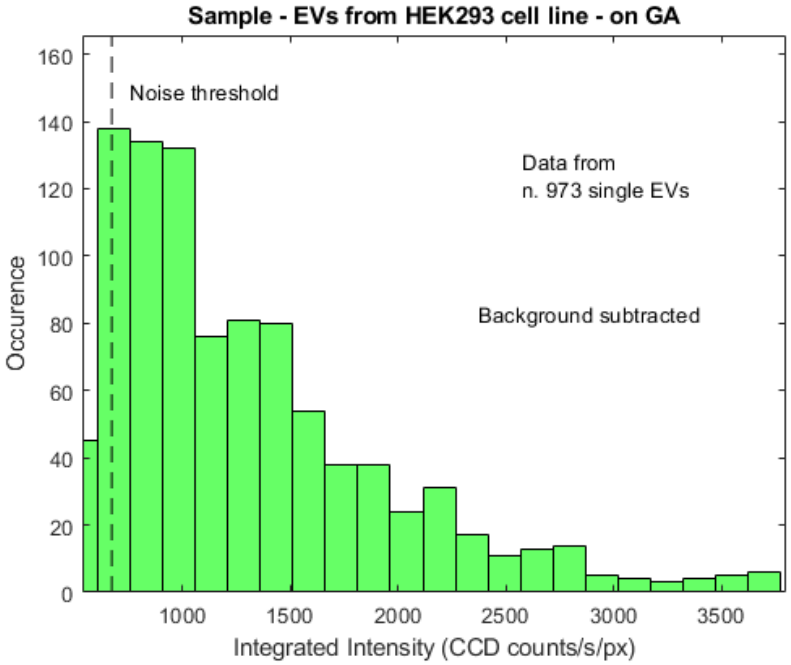

Figure 5.20: PL distribution of the background corrected integrated intensity of CD63-mNeonGFP tagged.

dard deviation of the background. This value may seem high but some factors must be taken into consideration to properly evaluate this parameter. First of all, as for the integrated intensity of the vesicle, also the value of the background increases. Moreover, due to the configuration of sample stage the can be used for the AFM measurements in liquid, it is not possible to have two distinct region for the sample and the control, but only a small free surface with a diameter smaller than $23\,mm$, for the sample investigation. Hence, the value of the background was calculated in the free areas of the substrate where no EVs were attached. Since this is not a very accurate method, the value indicated as noise can not be considered completely correct. Regarding the Integrated Intensity distribution, it can be seen that the number of the selected vesicles is consistently higher respect to the PL distributions illustrated in the *Section 5.1*, as it was adopted a higher concentration and it was investigated a bigger area. This helped to get statistical data for a great number of vesicles.

Focusing now on the AFM analysis, *Fig. 5.21* shows the AFM image of the substrate area of

$30 \times 30\,\mu m$ with the marks that will be used to realize the overlap with the marks in the PL image. It must be considered that the color range of the image, due to the low resolution of this preliminary scan, is not completely representative of the sample hight but it gives only a general idea of how the sample looks like.

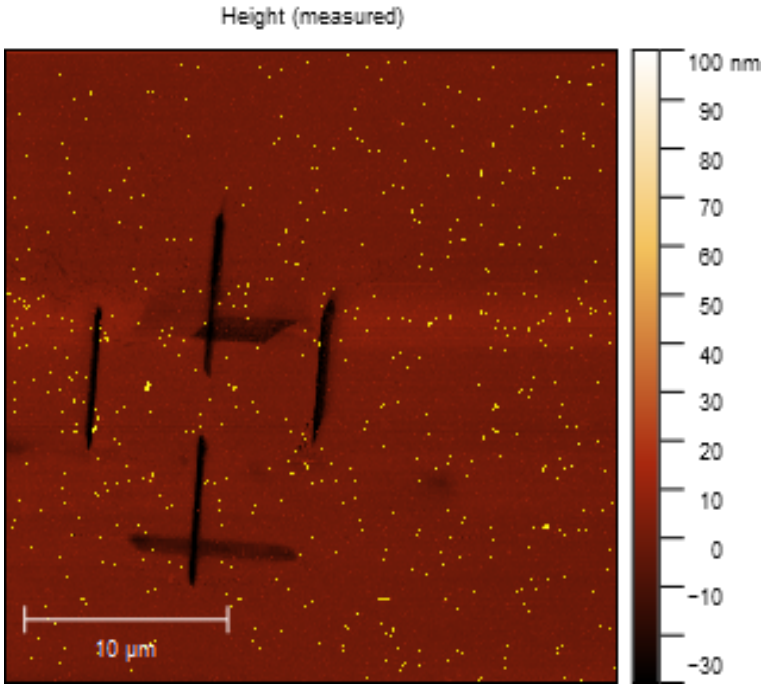

Figure 5.21: AFM image of a $30 \times 30\,\mu m$ area with mark

Starting from the low-resolution image shown in *Fig. 5.21* and the PL image illustrated in *Fig. 5.19*, the subsequent AFM images were overlapped using as reference points the edges of the marks, as shown as in *Fig. 5.22* that describes how the single images acquired from each step of the analysis were overlapped. In sequence we have *Fig. 5.22(a)* that represents the PL image of the vesicles attached on GA, then the *Fig. 5.22(b)* which is the low-resolution scan previously described, is superimposed to the PL image, thanks to the presence of the patterns, otherwise, it would be impossible to realize the correlation. After that, one other scan illustrated in *Fig. 5.22(c)*, of $10 \times 10\,\mu m$ and better resolution is taken in proximity to the marks, to obtain greater results about the heights of the sample. Finally, a consistent number of high-resolution AFM images, as shown in the *Fig. 5.22(d)*, with an area of $5 \times 5\,\mu m$, were acquired in those areas of the PL image characterized by a good focus of the vesicles.

Each of the high-resolution images was then analyzed in terms of height and radius distribution of the vesicles, considering now $10\,nm$ as threshold instead of $12\,nm$ because it was observed that the size of the diameter was underestimated due to the software calculation method. The software determines, based on the selected threshold, the coordinate of the maximum height and the equivalent disc radius of each grain. The former is calculated by considering the point of the grain with the maximum height above the threshold. The latter is determined respect to the coordinate of the maximum height which is considered as the center of a semi-ellipsoid and considering all the points of the grain having the hight above the threshold. Hence, all the points

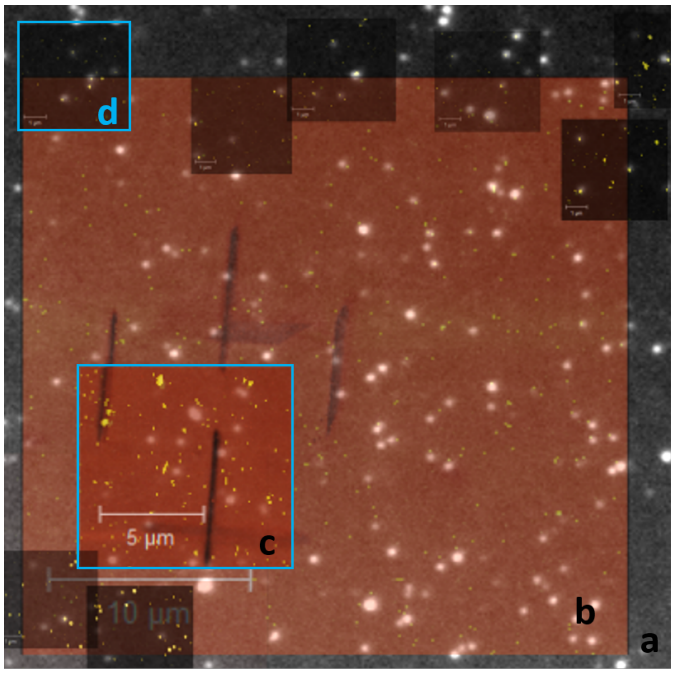

Figure 5.22: a. PL image; b. Low resolution AFM image with marks; c. AFM image with medium resolution with mark; d. AFM image of small areas with EVs at high resolution

under the threshold are excluded by the size estimation of the diameter, resulting in a loss of information. Since the diameter parameter is fundamental for the analysis that we want to carry out, it was decided to reduce the threshold to have a lower margin of error.

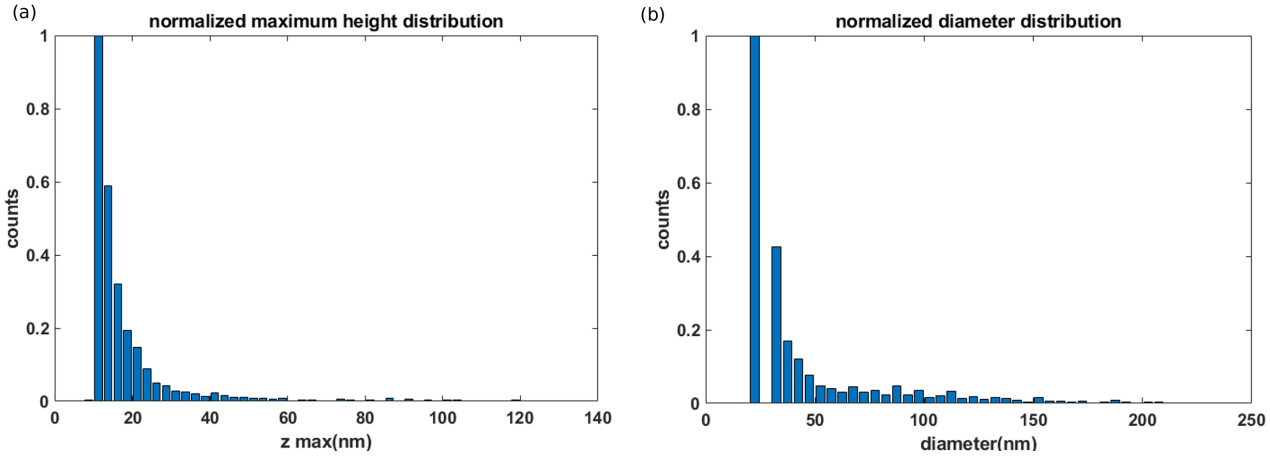

Figure 5.23: (a) Maximum Height and (b) Diameter - distribution of sEVs derived from the cell line HEK293 - fixed on GA.

Figure 5.23 illustrates the size distributions of the height and diameter of the vesicles analyzed with high resolution. Because of the higher number of data, both of the distributions show a greater

logarithmic trend, compared to the results illustrated in *Fig. 5.17* where especially the values of the diameter seemed to be more irregular throughout the size range. From the height distribution, shown in *Fig. 5.23(a)*) it can be observed that the majority of the vesicles reside in the range of $10 \div 25\,nm$ which is the common variation that as been observed in the other illustrated tests, whereas for what concerns the diameter distribution (shown in *Fig. 5.23(b)*) it seems that a great part of the vesicles has a typical size in the range of $20 \div 40\,nm$ confirming what was obtained previously.

Regarding the size correlation illustrated in *Fig. 5.24*, about the sEVs identified as single vesicle by the overlap of the AFM and PL images, it is possible to observe a linear distribution of the vesicles in the whole range, with the highest number of vesicles in the range of $40 \div 80\,nm$ in height and $80 \div 160\,nm$ in diameter.

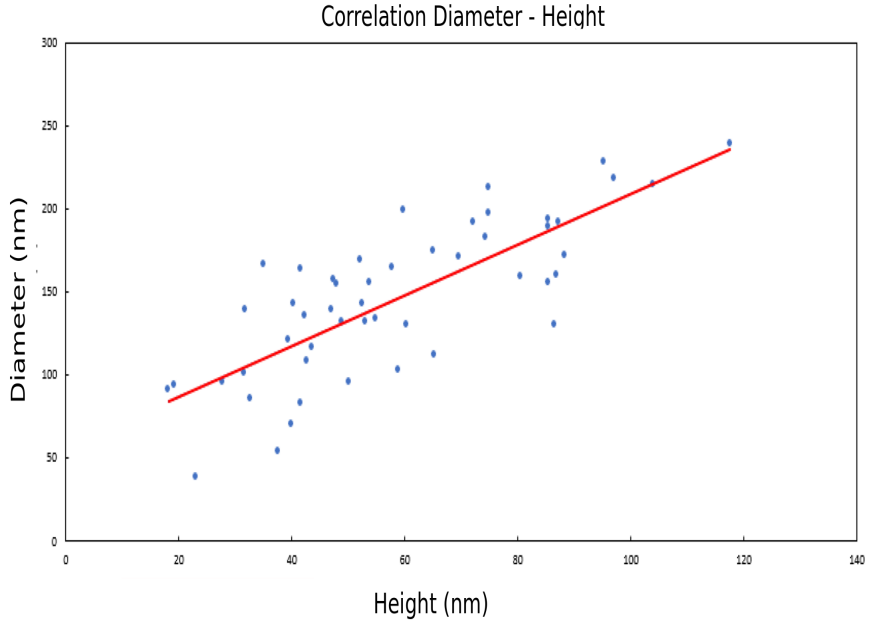

Figure 5.24: Correlation between the Height and Diameter of each vesicles.

Thus comparing the distributions of the total group of vesicles attached in the analyzed areas, with the results of the vesicles analyzed at the single-particle level, it can be seen their significant difference. By considering only the results of the first approach, it could be concluded that the sEVs derived from the HEK293 cell line varies in size in the two range mentioned above, without having any certainty that the vesicles analyzed are impurities, single EVs or clusters of multiple small EVs.

These problems can be solved by adopting the second approach based on the correlation between the two different techniques. From the PL image, it is indeed possible to distinguish the vesicles from all the rest attached on the substrate since they are the only component labeled with the fluorescent dye. On the other hand, after the overlap of the AFM image, it is also possible to characterize the size of the single identified vesicles, minimizing the error in the size distribution that otherwise would give only general information about the size of the vesicles, regardless of the surface protein expression level.

The correlation illustrated in *Fig. 5.24* between the height and the diameter was elaborated based on the single sEVs identified on both the PL and AFM images, as shown in *Fig. 5.25*.

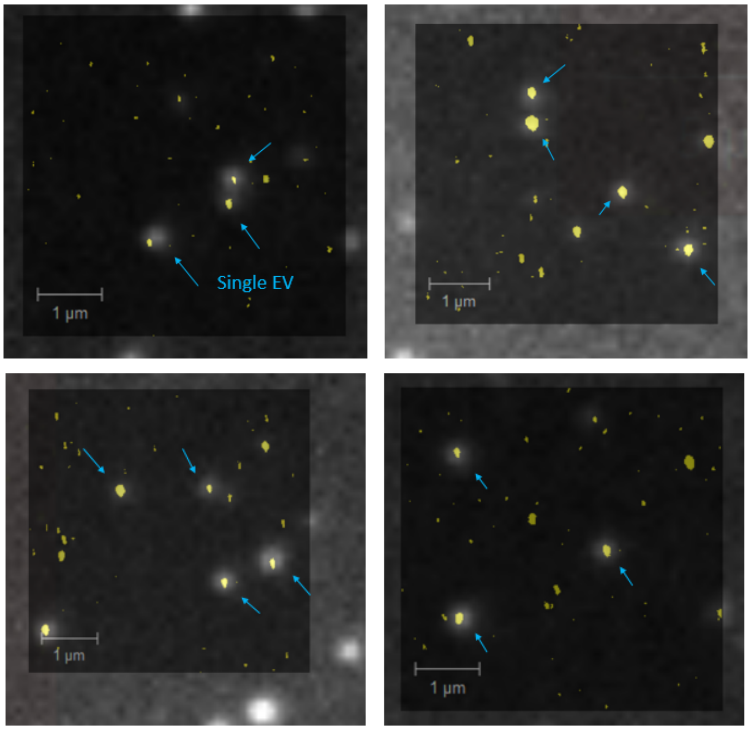

Figure 5.25: Identification of single sEVs (bright spots pointed by arrows) by overlapping of bright spots present in the PL (back) and AFM (front) images.

As a selection criterion, it was considered as single sEVs the only one with clear single dot overlapped, having the height and diameter in the typical range of the EVs, and with no other particles in their proximity characterized by the typical size of the EVs. All the vesicles of PL image that were identified by two or more vesicles in AFM image have not been taken into consideration, as the vesicles identified only in the AFM image have not been analyzed individually.
According to what has been observed so far, the last study of the project aims to figure out which correlation exists between the amount of CD63 protein (labeled by a mNeonGFP) of the single vesicles and their surface area. This information could be useful from the biomedical point of view because it is believed that the small particles could be more involved in the biological processes due to the small size that allows them to better communicate with the other cells and molecules. If that consideration is not true, we expect to have higher PL intensities in the vesicles with the bigger surface area just because of their size. If instead, the hypothesis was valid, we would expect to obtain the higher surface expression level in the smaller vesicles, and vice versa for the bigger ones.

Figure 5.26 shows the correlation between the PL intensity and the surface area of the vesicles, at the single-particle level. It can be seen that the fitted curve of the distribution does not start from the origin of the axis, but it intersects the y-axis at $670\,CCD\,counts/s/px$ that represents the noise threshold selected at the beginning during the PL analysis. Furthermore, the correlation

presents some point with a certain value of the area and a respective PL intensity equal to zero. This is related to the fact that it was assumed for those vesicles identified in the AFM image but characterized by a weak intensity from the PL analysis, that their intensity value would have been equal to the background. Since the illustrated PL intensities are background corrected, the value of those vesicles goes to $0\,CCD\,counts/s/px$.

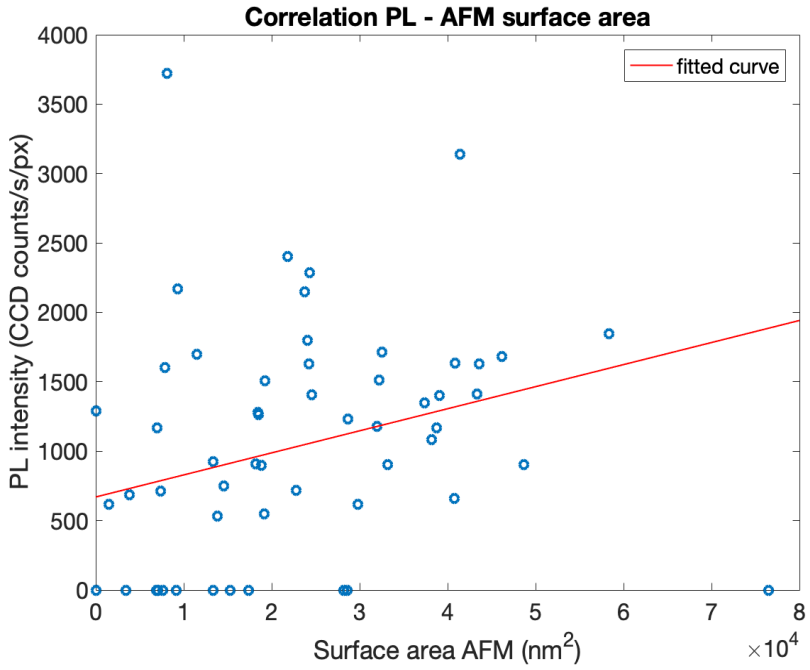

Figure 5.26: Correlation between the PL intensity of the single sEVs and the respective AFM Surface Area

From what emerges from the graph, it seems that the highest PL intensities are more concentrated in the medium-low values of the surface range, with only a few points for the medium-high values of the surface area, and in both cases, the values are spread respect to the linear fitting of the distribution. However, this phenomenon does not seems to be so pronounced and clear that it can be concluded that the smaller EVs have a pivotal role in the biological process and so their expression level is certainly higher respect to the bigger ones. To be able to have a better distribution that can highlight the different expression level and the consequent different roles of the vesicles, it is necessary first of all to collect a large number of data and also to make the sample preparation and the data analysis as much as possible operator-independent to be able to obtain better reproducible results.

Chapter 6

Conclusions and Future perspective

In this thesis, two different characterization methods have been investigated. The objective of the first study was to characterize the protein expression level of EVs by means of fluorescence microscopy. In particular, this was applied to the cell line HEK293 for the tetraspanin family proteins CD9 and CD63. The second part of the project aimed to characterize their size by AFM. Finally, the combination of the two techniques allowed us to carry out the single-particle analysis.

The principal goal of the project was to overcome the resolution limits of detection of the nanoscale-vesicle analysis, by using the Fluorescence Microscopy and Atomic-Force Microscopy, and their combination. As a consequence, initial evidence was highlighted from the biomedical point-of-view regarding the vesicle's behavior.

In the first part of the work, the surface protein expression level was successfully characterized by performing micro-photoluminescence measurements on an inverted microscope with two different excitation sources, a blu-LED for the CD63 protein and a red-laser for the CD9 expression level estimation. The use of the engineered cell-line HEK293 allowed us to realize a protocol for the optimization of the vesicle's fixation, concentration, and labeling with fluorescent dyes for their imaging with high resolution at the single-particle level. Thanks to the different labeling of the two proteins, CD63 tagged with mNeonGreen and CD9 labeled with AlexaFluor647, it was possible to realize the multiple bio-marker investigations. By comparing the results obtained with a different cell line, and with a different functionalization method it was possible to demonstrate the effectiveness of our characterization method.

In the second part of the work, the size and shape characterizations were realized with Atomic-Force microscopy measurements, adopting the quantitative imaging method. This allowed obtaining high-resolution images with the application of low forces and reduction of the vesicle damaging. Furthermore, the vesicle's fixation onto a glass substrate and their analysis in liquid, allowed to obtain high-quality images with partial shape preservation. It was observed that the vesicles are not spherical even if in liquid, but they present a semi-ellipsoid shape, with typical height in the range of $15 \div 30\,nm$ and a diameter in the range of $20 \div 160\,nm$. It was also observed that the use of antibodies as a linker between the vesicles and the substrate does not give significant improvements for the shape preservation, but it only mediates a more selective bounding. Hence, it was decided to realize all the single-vesicle characterization using the GA instead of antibodies, to reduce the time of sample preparation, have a lower roughness and to be able to collect more data for statistical analysis.

The last part of the thesis aimed to combine the AFM and the PL measurements, to overcome

the intrinsic uncertainty level of the average analysis of the EVs. Moreover, by correlating the size and the molecular profiling of the vesicles, it was possible to discover the relation existing between these two parameters. It was first observed that is not sufficient to use only one method of investigation to classify the EVs as single vesicles, since with the fluorescent imaging, two or more particles can appear as a single bright spot if they are sufficiently small and closed together, and from the size imaging, is not always possible to identify the vesicles from the other particles and impurities attached on the surface. With the overlap of the two images, it is instead possible to clearly localize the single vesicles on the substrate. Furthermore, by correlating the size and the molecular profile of every single vesicle, we discovered that does not seem to exist a clear difference between the protein expression level of the smallest and largest vesicles, suggesting that the size probably it is not a determinant factor in the vesicle's communication and their active role in the tumorigenesis processes progression.

The promising results obtained with the photoluminescence setup and its combination with the AFM, open the possibility for future improvements in the single-EV assay, with the main objective of realizing a multi-well system for the parallel analysis of the vesicles derived from different clinical samples and their comparison in terms of different size and protein expression level. Moreover, by increasing the number of fluorescent-probes it would be possible to realize for each clinical sample a multiple protein profiling, with the possibility to understand how the expression level of specific biomarkers change depending on the selected patient and its clinical condition.

Prior to the realization of the final objective, the next step in the study would be to apply the PL-AFM combined technique to cell line-derived wild-type EVs, where their protein expression levels are not engineered but naturally determined by the secreting cells. In this way, it would be possible to investigate whether these EVs show a similar/different relation between their size and protein expressions, and how the correlation change depending on the marker and cell line analyzed.

Bibliography

[1] Alexa fluor 647 dye. Available at https://www.thermofisher.com/it/en/home/life-science/cell-analysis/fluorophores/alexa-fluor-647.html.

[2] mneongreen at fpbase. Available at https://www.fpbase.org/protein/mneongreen/.

[3] Johnny C Akers, David Gonda, Ryan Kim, Bob S Carter, and Clark C Chen. Biogenesis of extracellular vesicles (ev): exosomes, microvesicles, retrovirus-like vesicles, and apoptotic bodies. *Journal of neuro-oncology*, 113(1):1–11, 2013.

[4] Samir EL Andaloussi, Imre Mäger, Xandra O Breakefield, and Matthew JA Wood. Extracellular vesicles: biology and emerging therapeutic opportunities. *Nature reviews Drug discovery*, 12(5):347–357, 2013.

[5] Annalisa Calò, David Reguera, Gerard Oncins, Marie-Annick Persuy, Guenhaël Sanz, Simona Lobasso, Angela Corcelli, Edith Pajot-Augy, and Gabriel Gomila. Force measurements on natural membrane nanovesicles reveal a composition-independent, high young's modulus. *Nanoscale*, 6(4):2275–2285, 2014.

[6] Sarah Caruso and Ivan KH Poon. Apoptotic cell-derived extracellular vesicles: more than just debris. *Frontiers in immunology*, 9:1486, 2018.

[7] Sara Cavallaro, Josef Horak, Petra Hååg, Dhanu Gupta, Christiane Stiller, Siddharth S Sahu, Andre Gorgens, Hithesh K Gatty, Kristina Viktorsson, Samir El Andaloussi, et al. Label-free surface protein profiling of extracellular vesicles by an electrokinetic sensor. *ACS sensors*, 4(5):1399–1408, 2019.

[8] Ching-Wei Chang, Dhruv Sud, and Mary-Ann Mycek. Fluorescence lifetime imaging microscopy. *Methods in cell biology*, 81:495–524, 2007.

[9] Chun-yi Chiang and Chihchen Chen. Toward characterizing extracellular vesicles at a single-particle level. *Journal of biomedical science*, 26(1):1–10, 2019.

[10] L Chopinet, C Formosa, MP Rols, RE Duval, and Etienne Dague. Imaging living cells surface and quantifying its properties at high resolution using afm in qi™ mode. *Micron*, 48:26–33, 2013.

[11] Giulia Corso, Wolf Heusermann, Dominic Trojer, André Görgens, Emmanuelle Steib, Johannes Voshol, Alexandra Graff, Christel Genoud, Yi Lee, Justin Hean, et al. Systematic characterization of extracellular vesicle sorting domains and quantification at the single molecule–single

vesicle level by fluorescence correlation spectroscopy and single particle imaging. *Journal of extracellular vesicles*, 8(1):1663043, 2019.

[12] Rebecca A Dragovic, Christopher Gardiner, Alexandra S Brooks, Dionne S Tannetta, David JP Ferguson, Patrick Hole, Bob Carr, Christopher WG Redman, Adrian L Harris, Peter J Dobson, et al. Sizing and phenotyping of cellular vesicles using nanoparticle tracking analysis. *Nanomedicine: Nanotechnology, Biology and Medicine*, 7(6):780–788, 2011.

[13] Vasco Filipe, Andrea Hawe, and Wim Jiskoot. Critical evaluation of nanoparticle tracking analysis (nta) by nanosight for the measurement of nanoparticles and protein aggregates. *Pharmaceutical research*, 27(5):796–810, 2010.

[14] Michael J Gerdes, Christopher J Sevinsky, Anup Sood, Sudeshna Adak, Musodiq O Bello, Alexander Bordwell, Ali Can, Alex Corwin, Sean Dinn, Robert J Filkins, et al. Highly multiplexed single-cell analysis of formalin-fixed, paraffin-embedded cancer tissue. *Proceedings of the National Academy of Sciences*, 110(29):11982–11987, 2013.

[15] Franz J Giessibl. Advances in atomic force microscopy. *Reviews of modern physics*, 75(3):949, 2003.

[16] Maria Cristina Lo Giudice, Luciana M Herda, Ester Polo, and Kenneth A Dawson. In situ characterization of nanoparticle biomolecular interactions in complex biological media by flow cytometry. *Nature communications*, 7(1):1–10, 2016.

[17] Cristina Grange, Marta Tapparo, Stefania Bruno, Devasis Chatterjee, Peter J Quesenberry, Ciro Tetta, and Giovanni Camussi. Biodistribution of mesenchymal stem cell-derived extracellular vesicles in a model of acute kidney injury monitored by optical imaging. *International journal of molecular medicine*, 33(5):1055–1063, 2014.

[18] Julia Gross, Sabrina Sayle, Anne R Karow, Udo Bakowsky, and Patrick Garidel. Nanoparticle tracking analysis of particle size and concentration detection in suspensions of polymer and protein samples: influence of experimental and data evaluation parameters. *European Journal of Pharmaceutics and Biopharmaceutics*, 104:30–41, 2016.

[19] Thomas A Hartjes, Serhii Mytnyk, Guido W Jenster, Volkert van Steijn, and Martin E van Royen. Extracellular vesicle quantification and characterization: common methods and emerging approaches. *Bioengineering*, 6(1):7, 2019.

[20] Mike Heilemann. Fluorescence microscopy beyond the diffraction limit. *Journal of biotechnology*, 149(4):243–251, 2010.

[21] Guosong Hong, Alexander L Antaris, and Hongjie Dai. Near-infrared fluorophores for biomedical imaging. *Nature Biomedical Engineering*, 1(1):1–22, 2017.

[22] JPK Instruments. The nanowizard afm handbook, 2005.

[23] Mehrnaz Izadpanah, Arshia Seddigh, Somayeh Ebrahimi Barough, Seyed Abolhassan Shahzadeh Fazeli, and Jafar Ai. Potential of extracellular vesicles in neurodegenerative diseases: diagnostic and therapeutic indications. *Journal of Molecular Neuroscience*, 66(2):172–179, 2018.

[24] Liangdi Jiang, Yongwei Gu, Yue Du, and Jiyong Liu. Exosomes: diagnostic biomarkers and therapeutic delivery vehicles for cancer. *Molecular pharmaceutics*, 16(8):3333–3349, 2019.

[25] Kyungheon Lee, Kyle Fraser, Bassel Ghaddar, Katy Yang, Eunha Kim, Leonora Balaj, E Antonio Chiocca, Xandra O Breakefield, Hakho Lee, and Ralph Weissleder. Multiplexed profiling of single extracellular vesicles. *ACS nano*, 12(1):494–503, 2018.

[26] Jing Li, Xianqing He, Yuanyuan Deng, and Chenxi Yang. An update on isolation methods for proteomic studies of extracellular vesicles in biofluids. *Molecules*, 24(19):3516, 2019.

[27] Jeff W Lichtman and José-Angel Conchello. Fluorescence microscopy. *Nature methods*, 2(12):910–919, 2005.

[28] Konstantin A Lukyanov, Dmitry M Chudakov, Sergey Lukyanov, and Vladislav V Verkhusha. Photoactivatable fluorescent proteins. *Nature Reviews Molecular Cell Biology*, 6(11):885–890, 2005.

[29] Irina Nazarenko. Extracellular vesicles: Recent developments in technology and perspectives for cancer liquid biopsy. In *Tumor Liquid Biopsies*, pages 319–344. Springer, 2020.

[30] Maria S Panagopoulou, Alastair W Wark, David JS Birch, and Christopher D Gregory. Phenotypic analysis of extracellular vesicles: a review on the applications of fluorescence. *Journal of Extracellular Vesicles*, 9(1):1710020, 2020.

[31] P Parisse, I Rago, L Ulloa Severino, F Perissinotto, E Ambrosetti, P Paoletti, M Ricci, AP Beltrami, D Cesselli, and L Casalis. Atomic force microscopy analysis of extracellular vesicles. *European Biophysics Journal*, 46(8):813–820, 2017.

[32] María Pascual, Francesc Ibáñez, Consuelo Guerri, et al. Exosomes as mediators of neuron-glia communication in neuroinflammation. *Neural regeneration research*, 15(5):796, 2020.

[33] Ivan Pelant and Jan Valenta. *Luminescence spectroscopy of semiconductors*. Oxford University Press, 2012.

[34] Howard R Petty. Fluorescence microscopy: established and emerging methods, experimental strategies, and applications in immunology. *Microscopy research and technique*, 70(8):687–709, 2007.

[35] Fuhao Qiao, Peng Pan, Jiaping Yan, Jing Sun, Yan Zong, Zhiyong Wu, Xiaoqin Lu, Na Chen, Rui Mi, Yongbin Ma, et al. Role of tumor-derived extracellular vesicles in cancer progression and their clinical applications. *International journal of oncology*, 54(5):1525–1533, 2019.

[36] Shima Rahmati, Fereshteh Shojaei, Ali Shojaeian, Leila Rezakhani, and Mehdi Banitalebi Dehkordi. An overview of current knowledge in biological functions and potential theragnostic applications of exosomes. *Chemistry and physics of lipids*, page 104836, 2019.

[37] Srinivasa M Salapaka and Murti V Salapaka. Scanning probe microscopy. *IEEE Control Systems Magazine*, 28(2):65–83, 2008.

[38] Nathan C Shaner, Gerard G Lambert, Andrew Chammas, Yuhui Ni, Paula J Cranfill, Michelle A Baird, Brittney R Sell, John R Allen, Richard N Day, Maria Israelsson, et al. A bright monomeric green fluorescent protein derived from branchiostoma lanceolatum. *Nature methods*, 10(5):407, 2013.

[39] Shivani Sharma, Kingshuk Das, JungReem Woo, and James K Gimzewski. Nanofilaments on glioblastoma exosomes revealed by peak force microscopy. *Journal of the Royal Society Interface*, 11(92):20131150, 2014.

[40] Shivani Sharma, Boyd M Gillespie, Viswanathan Palanisamy, and James K Gimzewski. Quantitative nanostructural and single-molecule force spectroscopy biomolecular analysis of human-saliva-derived exosomes. *Langmuir*, 27(23):14394–14400, 2011.

[41] Shivani Sharma, Haider I Rasool, Viswanathan Palanisamy, Cliff Mathisen, Michael Schmidt, David T Wong, and James K Gimzewski. Structural-mechanical characterization of nanoparticle exosomes in human saliva, using correlative afm, fesem, and force spectroscopy. *ACS nano*, 4(4):1921–1926, 2010.

[42] Rafal Szatanek, Monika Baj-Krzyworzeka, Jakub Zimoch, Malgorzata Lekka, Maciej Siedlar, and Jarek Baran. The methods of choice for extracellular vesicles (evs) characterization. *International journal of molecular sciences*, 18(6):1153, 2017.

[43] Yu-Ling Tai, Pei-Yu Chu, Bao-Hong Lee, Ko-Chien Chen, Chia-Yu Yang, Wen-Hung Kuo, and Tang-Long Shen. Basics and applications of tumor-derived extracellular vesicles. *Journal of biomedical science*, 26(1):35, 2019.

[44] Sanjukta Guha Thakurta and Anuradha Subramanian. Fabrication of dense, uniform aminosilane monolayers: A platform for protein or ligand immobilization. *Colloids and Surfaces A: Physicochemical and Engineering Aspects*, 414:384–392, 2012.

[45] Clotilde Théry, Kenneth W Witwer, Elena Aikawa, Maria Jose Alcaraz, Johnathon D Anderson, Ramaroson Andriantsitohaina, Anna Antoniou, Tanina Arab, Fabienne Archer, Georgia K Atkin-Smith, et al. Minimal information for studies of extracellular vesicles 2018 (misev2018): a position statement of the international society for extracellular vesicles and update of the misev2014 guidelines. *Journal of extracellular vesicles*, 7(1):1535750, 2018.

[46] E Van Der Pol, AG Hoekstra, A Sturk, Cornelis Otto, TG Van Leeuwen, and R Nieuwland. Optical and non-optical methods for detection and characterization of microparticles and exosomes. *Journal of Thrombosis and Haemostasis*, 8(12):2596–2607, 2010.

[47] Edwin Van der Pol, Anita N Böing, Paul Harrison, Augueste Sturk, and Rienk Nieuwland. Classification, functions, and clinical relevance of extracellular vesicles. *Pharmacological reviews*, 64(3):676–705, 2012.

[48] Els J Van Der Vlist, Esther NM Nolte, Willem Stoorvogel, Ger JA Arkesteijn, Marca HM Wauben, et al. Fluorescent labeling of nano-sized vesicles released by cells and subsequent quantitative and qualitative analysis by high-resolution flow cytometry. *Nature protocols*, 7(7):1311–1326, 2012.

[49] Xinyi Wang, Haiyang Zhang, Haiou Yang, Ming Bai, Tao Ning, Shuang Li, Jialu Li, Ting Deng, Guoguang Ying, and Yi Ba. Cell-derived exosomes as promising carriers for drug delivery and targeted therapy. *Current cancer drug targets*, 18(4):347–354, 2018.

[50] Peter Wolf. The nature and significance of platelet products in human plasma. *British journal of haematology*, 13(3):269–288, 1967.

[51] Yishi Wu, Yuhui Wang, Min Wei, Xiao Han, Tianmin Xu, and Manhua Cui. Advances in the study of exosomal lncrnas in tumors and the selection of research methods. *Biomedicine & Pharmacotherapy*, 123:109716, 2020.

[52] María Yáñez-Mó, Pia R-M Siljander, Zoraida Andreu, Apolonija Bedina Zavec, Francesc E Borràs, Edit I Buzas, Krisztina Buzas, Enriqueta Casal, Francesco Cappello, Joana Carvalho, et al. Biological properties of extracellular vesicles and their physiological functions. *Journal of extracellular vesicles*, 4(1):27066, 2015.

[53] MikoŁaj P Zaborowski, Leonora Balaj, Xandra O Breakefield, and Charles P Lai. Extracellular vesicles: composition, biological relevance, and methods of study. *Bioscience*, 65(8):783–797, 2015.

Appendix A

Sample Preparation

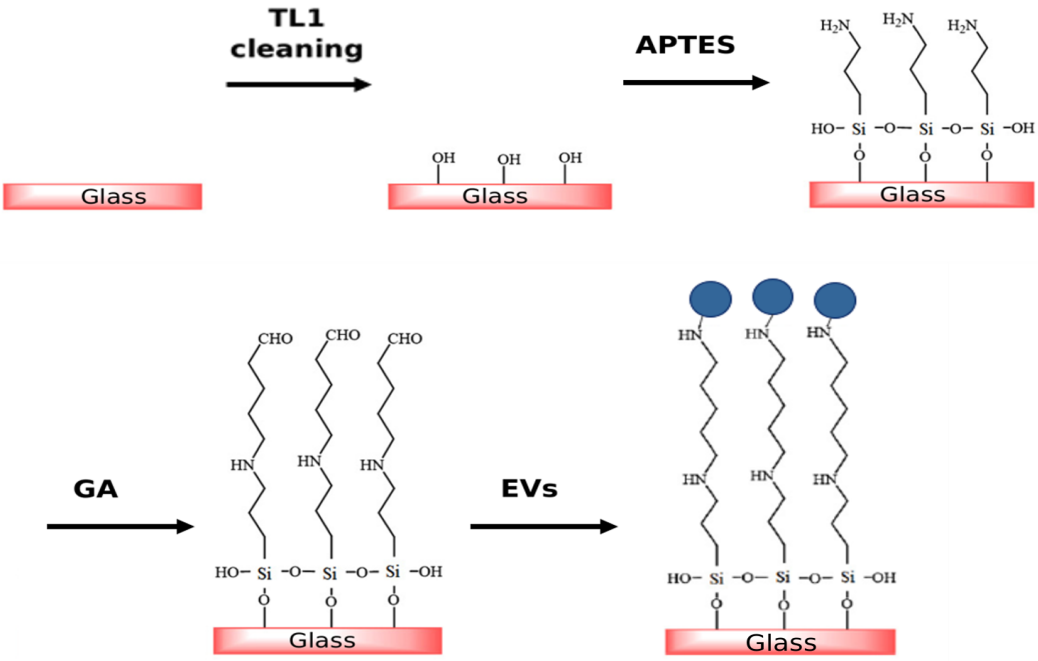

Figure A.1: Schematic representation of EVs capture on bio-chemically treated glass substrate using APTES and glutaraldehyde linker. The method involves: (a) substrate cleaning using TL1 solution; (b) generation of silane layer using optimized APTES $(5\%, v/v)$ solution; (c) treatment with glutaraldehyde solution; (d) immobilization of capture EVs.

Appendix B

Data used for the PL-AFM correlation

Table B.1: Data of single vesicles analyzed in the PL-AFM coorelation study

N.Vesicle	**Intensity** (CCD counts/s/px)	**Z max** (nm)	**Diameter** (nm)	**Surface** (nm^2)
1	42433.83	42.71	107.96	11478
2	40042.24	41.61	83.36	7826
3	15439.82	80.46	158.92	29814
4	23137.24	58.86	103.38	13377
5	17889.87	86.49	130.38	22778
6	17171.99	39.93	69,9	3815
7	33723.18	97.15	218.2	37384
8	35064.46	59.88	199.56	37384
9	22468,08	40,29	142,82	18838
10	22643,12	69,7	170,72	33152
11	35265,85	74,84	197,12	43316
12	27147,96	74,42	183,06	38156
13	32031,43	42,4	135,86	18403
14	78411,60	85,43	189,58	41379
15	13255,03	43,61	116,62	13799
16	15429,04	23,1	38,18	1491
17	45020,49	41,57	163,44	24099
18	29498,89	85,45	155,84	31966
19	31527,65	54,83	134,06	18501
20	17796,51	19,32	93,5	7408

N.Vesicle	**Intensity** (CCD counts/s/px)	**Z max** (nm)	**Diameter** (nm)	**Surface** (nm^2)
21	42809,97	86,98	160,44	32508
22	30773,92	52,17	169,28	28680
23	40799,51	95,27	228	40817
24	42080,96	85,43	193,38	46163
25	40687,53	87,3	192,12	43621
26	35108,95	53,77	155,84	24577
27	22598,00	74,94	212,6	48687
28	46164,73	104	214,8	58374
29	53660,29	47,97	154,28	23761
30	40786,80	47,39	157,38	24217
31	54204,27	31,65	101	9335
32	37694,10	53,16	132,24	19262
33	13649,89	47,07	139,38	19191
34	93048,62	27,76	96,06	8091
35	29202,63	18,2	90,86	6937
36	57096,74	35,12	166,38	24288
37	29184,15	88,3	172,12	38784
38	18745,47	39,37	120,72	14532
39	60068,37	52,48	142,82	21807
40	16475,28	72,24	192,12	40759
41	37848,55	65,05	174,92	32247
42	22756,63	48,86	132,24	18211,00